

https://dspace.org/

Analysis of EyringPowell hybrid nanofluid flow with magnetic dipole over a stretching sheet

Kazeem B. Kasali; Matthew O. Lawal; Musawenkosi P. Mkhatshwa; Y Tijani; Olumuyiwa Otegbeye

https://hdl.handle.net/10539/46476
WOS

Downloaded from a DSpace repository. https://dspace.org/

Modeling Earth Systems and Environment (2025) 11:396
https://doi.org/10.1007/s40808-025-02580-z

ORIGINAL ARTICLE

Analysis of Eyring-Powell hybrid nanofluid flow with magnetic dipole over a stretching sheet

Kazeem B. Kasali[1] · Matthew O. Lawal[2] · Musawenkosi P. Mkhatshwa[3] · Yusuf O. Tijani[4] · Olumuyiwa Otegbeye[5]

Received: 22 May 2025 / Accepted: 6 August 2025
© The Author(s) 2025

Abstract
Stretching surfaces under localized magnetic fields, such as magnetic dipoles, enhance the thermal management and materials processing applications across industries. This study presents a numerical analysis of the boundary layer flow, heat, and mass transfer characteristics of an Eyring-Powell hybrid nanofluid over a linearly stretching sheet, incorporating the significant effects of a magnetic dipole. The governing non-linear partial differential equations describing the conservation of mass, momentum, energy, and nanoparticle concentration are transformed into a system of coupled two-variable differential equations using appropriate non-similarity transformation techniques. Due to the complexity and non-linearity of the resulting system, a robust numerical approach, the bivariate pseudospectral method, is used to obtain accurate solutions. The efficacy and convergence of the numerical scheme are rigorously demonstrated through the presentation and analysis of residual error and solution error plots respectively, confirming the reliability of the obtained results. The numerical investigation explores the impact of various pertinent parameters on the fluid velocity, temperature, and concentration profiles, as well as the associated skin friction coefficient, Nusselt number, and Sherwood number. It is notably observed that increasing the distinct Eyring-Powell fluid parameters yields contrasting effects on the drag force experienced at the sheet surface. Furthermore, the analysis reveals that both the Biot number and the thermal radiation parameter exert qualitatively similar enhancing influences on the rate of heat transfer from the fluid to the stretching sheet wall. This work provides valuable insights into the complex interplay of non-Newtonian rheology, magnetic dipole effects, and hybrid nanoparticle transport in boundary layer flows.

Keywords Magnetic Dipole · Eyring-Powell · Differential equation · Spectral collocation method · Hybrid Nanofluid

List of symbols

Latin symbols

u, v	Velocity field components $(\mathrm{m\ s^{-1}})$
x, y	Cartesian coordinates (m)
K_r	Reaction rate coefficient $(\mathrm{s^{-1}})$
M	Magnetization $(\mathrm{A\ m^{-1}})$
H	Magnetic field density $(\mathrm{A\ m^{-1}})$
T	Temperature (K)
C	Concentration $(\mathrm{mol\ m^{-3}})$

✉ Kazeem B. Kasali
kazeem.kasali@tech-u.edu.ng

✉ Yusuf O. Tijani
olodyusuf@gmail.com

Matthew O. Lawal
femathlaw@yahoo.com

Musawenkosi P. Mkhatshwa
musawenkosi.mkhatshwa@ul.ac.za

Olumuyiwa Otegbeye
olumuyiwa.otegbeye@wits.ac.za

[1] Department of Mathematics and Statistics, Abiola Ajimobi Technical University, Ibadan, Nigeria

[2] Department of Mathematics, Adeyemi Federal University of Education, Ondo P.M.B. 520, Ondo, Nigeria

[3] Department of Mathematics and Applied Mathematics, University of Limpopo, Private Bag X1106, Sovenga 0727, South Africa

[4] Department of Mathematics, Rhodes University, Makhanda, PO Box 94, Grahamstown 6140, South Africa

[5] School of Computer Science and Applied Mathematics, University of the Witwatersrand, Private Bag 3, Braamfontein, Johannesburg 2050, South Africa

Published online: 20 August 2025

T_∞	Temperature away from the sheet (K)
C_∞	Ambient concentration ($\mathrm{mol\ m^{-3}}$)
T_w	wall temperature (K)
k'	Mean absorption coefficient ($\mathrm{m^{-1}}$)
C_w	Wall concentration ($\mathrm{mol\ m^{-3}}$)
c_p	Specific heat capacity ($\mathrm{J\ kg^{-1}\ K^{-1}}$)
D_B	Mass diffusivity ($\mathrm{m^2\ s^{-1}}$)
q_a	Uniform heat flux ($\mathrm{kg\ m\ s^{-3}}$)
k	Thermal conductivity ($\mathrm{kg\ m\ s^{-3}\ K^{-1}}$)
h_f	Heat transfer coefficient ($\mathrm{W\ m^{-2}\ K^{-1}}$)
U_w	Wall velocity ($\mathrm{m\ s^{-1}}$)
U_∞	Free stream velocity ($\mathrm{m\ s^{-1}}$)
Cf_x	Skin friction coefficient
a	constant representing plate velocity ($\mathrm{s^{-1}}$)
Nu_x	Local Nusselt number
f	Dimensionless stream function
Sh_x	Local Sherwood number
L	Characteristic length (m)
ω_1, ω_2	Material constants
k_m	permeability of porous media ($\mathrm{m^2}$)
q_r	Local radiative heat flux ($\mathrm{W\ m^{-2}}$)
q_b	Uniform mass flux ($\mathrm{mol\ m^{-2}\ s^{-1}}$)

Greek symbols

λ_0	Magnetic permeability ($\mathrm{kg\ m\ A^{-2}\ s^{-2}}$)
ν	Kinematic viscosity ($\mathrm{m^2\ s^{-1}}$)
μ	Dynamic viscosity ($\mathrm{kg\ m^{-1}\ s^{-1}}$)
θ	Non-dimensional temperature
φ	Non-dimensional concentration
σ'	Stefan-Boltzmann constant ($\mathrm{W\ m^{-2}\ K^{-4}}$)
ψ	Stream function ($\mathrm{m^2\ s^{-1}}$)
τ_w	wall shear stress ($\mathrm{kg\ m^{-1}\ s^{-2}}$)
ϕ_1, ϕ_2	Solid volume fraction of Fe_2O_3 and Al_2O_3
ρ	Density ($\mathrm{kg\ m^{-3}}$)
η, ξ	Transformed variables

Subscripts

w, ∞	Wall and ambient conditions
f	Fluid
$p1, p2$	Solid nanoparticles of Fe_2O_3 and Al_2O_3
nf, *hnf*	Single and hybrid nanofluids

Introduction

The study of fluid flow is fundamental to understanding a vast array of natural phenomena and technological systems, ranging from large-scale ocean currents and weather patterns to micro-level biological transport and advanced industrial processes (Kundu et al. 2016). Efficient heat transfer, mass transport, and momentum exchange, all governed by fluid mechanics principles, dictate the performance and feasibility of countless applications, including energy generation, chemical processing, materials manufacturing, electronics cooling, and biomedical devices (White 2006). Consequently, accurately predicting and controlling fluid behaviour is paramount for optimizing efficiency, ensuring safety, and driving innovation across diverse scientific and engineering fields. However, many fluids utilized in these critical applications do not adhere to the simple linear relationship between stress and strain rate defined by Newtonian models (Ireka 2015). These non-Newtonian fluids, including couple stress fluid (Jat et al. 2025b), Casson fluid (Jat et al. 2025b), micropolar fluid (Vaishnav et al. 2025), and Maxwell fluid (Nahlia et al. 2025), exhibit complex rheological behaviours that demand more sophisticated descriptions (Akolade and Tijani 2021; Tijani et al. 2022). Among the various non-Newtonian models, the Eyring-Powell fluid model garners significant attention due to its robust theoretical foundation in the kinetic theory of liquids and its versatility (Ogunseye and Sibanda 2019). The Eyring-Powell model is grounded in molecular theory rather than relying on empirical relationships, which is common for most non-Newtonian fluids. In contrast to the non-Newtonian fluids such as Casson model, which includes yield stress, the Eyring-Powell model effectively describes smooth shear-thinning behaviour without the presence of yield stress. The distinct advantage of Eyring-Powell model lies in its ability to accurately capture the rheology of fluids that exhibit both shear-thinning (viscosity decreases with shear rate) and shear-thickening (viscosity increases with shear rate) behaviour across a broad spectrum of shear rates, from very low to very high. This makes the Eyring-Powell model particularly relevant and important for analyzing processes involving polymer solutions, certain industrial slurries, lubricants, and biological fluids where simpler models like the power-law model may prove to be inadequate at the extremes of shear rate, thereby enabling more realistic simulations and better design of relevant systems (Wajihah and Sankar 2023). It is noteworthy that the Eyring-Powell model has demonstrated better alignment with experimental data in various engineering and biomedical applications, especially where thermal effects or pressure dependent viscosity play a significant role.

Nanofluids are engineered colloidal suspensions representing a significant step forward in heat transfer technology (Choi 1995). They are created by dispersing minuscule particles, typically ranging from 1 to 100 nanometers in size, within a conventional host liquid such as water, oil, or ethylene glycol (Ogunseye et al. 2020). The suspended nanomaterials can vary widely, including metals (*Cu*, *Ag*, *Au*, etc), various metal oxides (Al_2O_3, CuO, TiO_2, etc), carbides like *SiC*, or different forms of carbon (such as nanotubes or graphene). The fundamental advantage driving the

development of nanofluids is their capacity for substantially improved thermophysical properties, particularly thermal conductivity, which enables more effective heat transfer compared to the base fluid alone (Ogunseye and Sibanda 2019). The synergistic combination of enhanced thermal and mass transport capabilities inherent in nanofluids (hybrid nanofluid), alongside their practical applicability in industry, explains why their study is now so prevalent among researchers (Devi and Devi 2017; Gholinia et al. 2018). Investigations frequently delve into the complexities of nanofluid dynamics, aiming to optimize their performance in various flow-related applications (Ogunseye et al. 2021; Mkhatshwa et al. 2020). Walelign and Seid (2024) explored the effects of nanofluid in enhancing the heat transfer rate of micropolar fluid with the aid of the Buogiorno model. The emerging dimensionless model was solved using the optimal homotopy analysis method. It was shown that the presence of the Soret number, the Dufour number, and the micropolar fluid parameter contributes to an increase in the rate of heat transfer of the fluid. Jat et al. (2025a) utilized the Buongiorno nanofluid model to scrutinize magnetized flow, heat and mass transfer of a nanofluid in the presence of gyrotactic microorganisms, Darcy-Forchheimer model, heat generation/absorption and thermal radiation through a nonlinearly stretchable surface. However, Choudhary et al. (2025) employed the Tiwari-Das nanofluid model to investigate the impact of shape factor and alumina nanoparticles on the flow and thermal transfer of water-based nanofluid over a flat surface in the presence of magnetic field, porous media, viscous dissipation, and velocity slip effect. It was reported that greater nanoparticle volume fraction leads to enhanced fluid velocity while higher porosity parameter results in improved temperature dissemination.

In fluid dynamics, particularly magnetohydrodynamics (MHD) or ferrohydrodynamics (FHD), external magnetic fields are often applied to influence the flow behavior, heat transfer, and mass transfer characteristics. The magnetic dipole is a specific type of localized, non-uniform magnetic field source (Tijani et al. 2023a). Odenbach (2003) explained the importance of ferromagnetic fluid with the application of magnetic dipoles and magnetic control. The study by Odenbach (2003) shows that thermomagnetic and magnetoviscous effects are part of magnetic control mechanism. Hayat et al. (2003) investigated the influence of magnetic dipole on the flow of Williamson fluid subjected to a radiative effect in a stretching sheet and found that increasing the magnetic dipole parameter downsizes the flow rate of the fluid. The analysis of a magnetic dipole and thermal radiation impact on a viscous ferrofluid was investigated by Zeeshan et al. (2016). The study by Zeeshan et al. (2016) showed that both the velocity and temperature profiles have differing trajectories as the ferromagnetic parameter increases. Gontijo and Cunha (2017) investigated how a magnetic dipole interacts with flow-driven phenomena, such as thermal fluctuations and gravitational force, within a magnetic suspension. Their study showed that collective hydrodynamic mechanisms have a dispersive effect, which opposes the collective influence of magnetic dipole-dipole interactions. Awgichew et al. (2020) presented an analytical solution adopting the homotopy analysis method to examine the heat and mass transfer of an unsteady two-dimensional Williamson nanofluid within a porous medium. The study considered the influences of thermal radiation, magnetic field, and chemical reactions. The results revealed that the presence of the magnetic field parameter diminished the fluid velocity while simultaneously enhancing the temperature and concentration profiles of the fluid. Walelign (2025) probed the significance of magnetic field, thermal radiation, and heat source/sink on the heat transfer phenomenon of Casson nanofluid over an elastic sheet. For more perspectives, see Waleign et al. (2020); Kasali and Ajadi (2025); Haile et al. (2022).

Given the inherent complexity arising from the coupled, non-linear deterministic differential equations, obtaining a closed-form analytical solutions is often infeasible (Adomian 1994; Liao 2012). Consequently, researchers heavily rely on robust numerical methods to obtain approximate yet highly accurate solutions that provide valuable insights into the system's behaviour (Trefethen 2000). Various powerful numerical techniques have been developed and adapted for fluid flow problems, including the finite difference methods (FDMs) (Makinde and Chinyoka 2013; Takemitsu 1985; Javed et al. 2013), which approximates derivatives on a discretized grid, the finite element methods (FEMs), adept at handling complex geometries (Ibrahim and Lamesse 2023), and the finite volume methods (FVMs), particularly suited for problems where conservation laws are critical. Among these numerical techniques, spectral methods stand out for its potential to achieve very high accuracy (often exponential convergence) for problems with smooth solutions, primarily by representing the solution as a truncated series of basis functions (Chebyshev or Legendre polynomials) (Trefethen 2000; Canuto et al. 2006). However, the inherent nonlinearity of the governing fluid flow equations necessitates specialized iterative approaches when employing spectral discretization. Techniques such as the spectral quasi-linearization method (SQLM) tackle this by combining spectral collocation with the quasi-linearization (Newton–Raphson based) technique, transforming the non-linear system into a sequence of linear differential equations solved iteratively (Magagula et al. 2020; Otegbeye et al. 2020). Similarly, the spectral local linearization method (SLLM) offers an alternative iterative linearization strategy within the spectral framework, potentially improving convergence for highly

non-linear problems by linearizing locally (Motsa 2015, 2013; Tijani et al. 2023b). Other sophisticated spectral-based iterative techniques include the spectral relaxation method (SRM), which decouples the system and solves iteratively, and methods combining spectral discretization with domain decomposition or iterative coupling strategies (sometimes referred to as spectral overlapping techniques when dealing with domain decomposition) (Mkhatshwa et al. 2020). Single-domain pseudospectral methods, while highly accurate, often generate dense matrices. This can lead to significant computational challenges, particularly for large-scale problems, in terms of both processing time and memory demands. Domain decomposition techniques offer a powerful strategy to mitigate these issues. By partitioning the primary computational domain into smaller, more manageable subdomains, these methods inherently reduce the size of the matrices handled at any one time. This subdivision not only curtails memory requirements but also naturally lends itself to parallel processing architectures, further accelerating computations. The application of pseudospectral methods within domain decomposition frameworks has been an active area of research (Mkhatshwa et al. 2020). Specifically, extensive studies have explored their implementation in both overlapping and non-overlapping subdomain configurations, thoroughly investigating aspects such as numerical stability, convergence rates, and overall computational efficiency to optimize performance. These advanced numerical schemes are indispensable tools, enabling the detailed investigation of complex fluid flow phenomena and providing the quantitative predictions necessary for engineering design and scientific understanding where analytical approaches fall short (Ansari et al. 2021).

To the best of the authors' knowledge, a thorough and detailed analysis investigating the intricate fluid dynamics resulting from the interplay between magnetic dipole effects and Eyring-Powell fluid flow over a stretching sheet has not been documented in the existing literature. This work aims to fill the gap in understanding non-Newtonian fluid behaviour under the influence of magnetic fields. Specifically, a numerical simulation was developed that meticulously captures the complex interactions and nuances inherent in this particular flow scenario. By addressing these dynamics, this study not only enriches the theoretical framework surrounding Eyring-Powell fluids in magnetic environments but also opens new avenues for practical applications in various engineering and industrial processes.

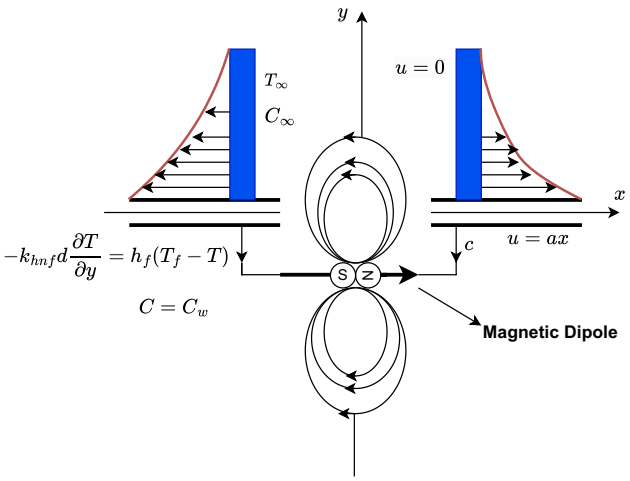


Fig. 1 Geometrical configuration of the flow

Model formulation analysis

Consider the flow of a steady 2-dimensional Eyring-Powell fluid over a stretching surface, subject to the combined effects of magnetic dipole dynamics, heat source and Arrhenius chemical reaction with nanoparticle effects. The fluid movements are largely supported by the stretching of the sheet and the magnetic dipole, see Fig. 1. The fluid has the suspension of two nanoparticles; as such the fluid is a hybrid nanofluid type. The fluid exhibits thermal sensitivity, meaning it is influenced by temperature, thus the conservation of energy is accounted for. The magnetic dipole is considered in the momentum and energy equations as in Tijani et al. (2023a)

$$\lambda_o M\frac{\partial H}{\partial x} \quad \text{and} \quad \lambda_o T\frac{\partial M}{\partial T}\left(u\frac{\partial H}{\partial x}+v\frac{\partial H}{\partial y}\right), \tag{2.1}$$

respectively, where $M = K_1(T_\infty - T)$ is the magnetization, λ_o stands for magnetic permeability, and H represent magnetic field intensity. Consequently, the magnetic field significantly impacts the conservation of energy equation, influencing heat transfer and fluid flow behaviour. The external influence of Darcy-Forchiemer and Hall effect are considered negligible in this study. The Darcy-Forchheimer model describes the resistance encountered by fluid flow through a porous medium. However, this study focuses specifically on the interactions of a magnetic field (in particular, a magnetic dipole) over porous resistance. Hence, Darcy-Forchheimer is not accounted for. Additionally, the Hall effect becomes significant when the magnetic field is strong. For this study, we examine the influence of the magnetic dipole on fluid flow while neglecting the Hall effect to prevent any overlap with the magnetic influence. The non-constant heat source follows the definition given in Sandeep and Sulochana (2018)

$$\frac{k_{hnf}U_w}{x\nu_{hnf}}\left[H_a(T_w - T_\infty)f' + H_b(T - T_\infty)\right], \tag{2.2}$$

where $H_a,\ H_b \in (0,\infty)$ indicates the scenario of heat generation, whereas the case of heat absorption is given as $H_a,\ H_b \in (-\infty,0)$.

The conservation equations for the aforementioned dynamics are given as (see Lawal et al. (2022) and Tijani et al. (2023a))

$$\frac{\partial u}{\partial x}+\frac{\partial v}{\partial y}=0, \tag{2.3}$$

$$\begin{aligned} u\frac{\partial u}{\partial x}+v\frac{\partial u}{\partial y} &= \frac{1}{\rho_{hnf}}\left(\mu_{hnf}+\frac{1}{\omega_1\omega_2}\right)\frac{\partial^2 u}{\partial y^2} \\ &- \frac{1}{2\rho_{hnf}\omega_1\omega_2^3}\left(\frac{\partial u}{\partial y}\right)^2\frac{\partial^2 u}{\partial y^2}+\frac{\lambda_o}{\rho_{hnf}}M\frac{\partial H}{\partial x}-\frac{\mu_{hnf}}{\rho_{hnf}k_m}u, \end{aligned} \tag{2.4}$$

$$\begin{aligned} (\rho c_p)_{hnf}\left(u\frac{\partial T}{\partial x}+v\frac{\partial T}{\partial y}\right) &= k_{hnf}\frac{\partial^2 T}{\partial y^2}-\frac{\partial q_r}{\partial y} \\ &+ \frac{k_{hnf}U_w}{x\nu_{hnf}}\left[H_a(T_w-T_\infty)f'+H_b(T-T_\infty)\right] \\ &- \lambda_o T\frac{\partial M}{\partial T}\left(u\frac{\partial H}{\partial x}+v\frac{\partial H}{\partial y}\right)+\mu_{hnf}\left[1+\frac{1}{\mu_{hnf}\omega_1\omega_2}\right. \\ &\left.- \frac{1}{2\mu_{hnf}\omega_1\omega_2^3}\left(\frac{\partial u}{\partial y}\right)^2\right]\left(\frac{\partial u}{\partial y}\right)^2, \end{aligned} \tag{2.5}$$

$$u\frac{\partial C}{\partial x}+v\frac{\partial C}{\partial y}=D_B\frac{\partial^2 C}{\partial y^2}-K_r(C-C_\infty)\exp\left(\frac{-E_a}{R_aT}\right), \tag{2.6}$$

where the notations or symbols are provided in the nomenclature section. Taking into account Rosseland approximation for thermal radiation and utilizing the optically thick medium, the radiation flux term q_r is expressed as follows Mkhatshwa (2024):

$$q_r=-\frac{4\sigma'}{3k'}\frac{\partial T^4}{\partial y}=-\frac{16\sigma'}{3k'}T^3\frac{\partial T}{\partial y}, \tag{2.7}$$

where σ' and k' represent Stefan-Boltzmann constant and Rosseland mean absorption coefficient, respectively. Differentiating the above heat flux equation (2.7), we obtain the next nonlinear radiative heat flux

$$\frac{\partial q_r}{\partial y}=-\frac{16\sigma'}{3k'}\frac{\partial}{\partial y}\left(T^3\frac{\partial T}{\partial y}\right), \tag{2.8}$$

which is then substituted in the energy equation. It is worth noting that this nonlinear radiation term enhances the accuracy of thermal boundary layer models when compared to the linearized version and it is utilized when the temperature difference is large and thermal radiation is strong. The suitable boundary conditions are given as

$$\begin{aligned} u &= ax, \quad v=0, \quad -k_{hnf}\frac{\partial T}{\partial y} \\ &= h_f(T_f-T), \quad C=C_w, \quad at \quad y=0. \end{aligned} \tag{2.9}$$

$$\begin{aligned} &u\to 0, \quad v\to 0, \quad T\to T_\infty, \\ &C\to C_\infty, \quad as \quad y\to\infty, \end{aligned} \tag{2.10}$$

where h_f represents the convective heat transfer coefficient. It is worth noting that the thermal boundary at the stretching sheet is described through the convective condition to reflect the heat exchange with external medium below the surface. This condition characterizes the simultaneous impact of heat conduction in the nanofluid layer and convection from the neighboring environment. This Robin-type condition finds applications in situations where the surface temperature fluctuates dynamically rather than being prescribed, and that is owed to the joint impact of conductive and convective heat transport. The slip velocity and thermal jump influences are ignored since they are typically appreciable only at micro or nanoscale dimensions. The dynamics of the magnetic dipole make the use of a similarity transformation not admissible. Therefore, we introduce a non-similar variable transformation given as

$$\begin{aligned} &\eta=y\sqrt{\frac{U_\infty}{\nu_f x}}, \quad u=\frac{\partial\psi}{\partial y}, \quad v=-\frac{\partial\psi}{\partial x}, \quad \xi=\frac{x}{L}, \\ &\psi=(U_\infty\nu_f x)^{\frac{1}{2}}f(\xi,\eta), \quad \theta=\frac{T-T_\infty}{T_w-T_\infty}, \\ &\varphi=\frac{C-C_\infty}{C_w-C_\infty}. \end{aligned} \tag{2.11}$$

Implementing equation (2.11) on equations (2.3) - (2.6) and the boundary conditions (2.9) - (2.10), we have the following equations:

$$\begin{aligned} &\left(1+\frac{\lambda_a}{\zeta_1}\right)f'''-\frac{\lambda_a\lambda_b}{\zeta_1}f''^2f'''-\mathcal{K}f'-\frac{\Delta_1}{\zeta_1}\frac{2\theta}{(\eta+\alpha_a)^4} \\ &+\frac{\zeta_2}{2\zeta_1}ff''+\frac{\zeta_2}{\zeta_1}\xi\left(f''\frac{\partial f}{\partial\xi}-f'\frac{\partial^2 f}{\partial\xi\partial\eta}\right)=0. \end{aligned} \tag{2.12}$$

$$\begin{aligned} &\theta''+\frac{4R}{3\zeta_3}\left[3\left(1+(T_R-1)\theta\right)^2(T_R-1)\theta'^2\right. \\ &\left.+(1+(T_R-1)\theta)^3\theta''\right]+\frac{\zeta_2}{\zeta_1}\left(H_af'+H_b\theta\right)+\frac{\zeta_4 Pr}{2\zeta_3}f\theta' \\ &+\frac{EcPr}{\zeta_3}\left(\zeta_1+\lambda_a-\lambda_a\lambda_b f''^2\right)f''^2 \\ &-\frac{2\Gamma_a\Delta_1\Delta_2}{\zeta_3}\left[\frac{\theta-\epsilon_a}{(\eta+\alpha_a)^4}\right]f'-\frac{\xi\zeta_4 Pr}{\zeta_3}\left(f'\frac{\partial\theta}{\partial\xi}-\frac{\partial f}{\partial\xi}\theta'\right) \\ &+\frac{\Delta_1\Delta_2}{\zeta_3}\left[\frac{4\Gamma_a(\theta-\epsilon_a)}{(\eta+\alpha_a)^5}-\frac{2(\theta-\epsilon_a)}{(\eta+\alpha_a)^3}\right]\left(\frac{\eta}{2}f'\right. \\ &\left.-\frac{1}{2}f-\xi\frac{\partial f}{\partial\xi}\right)=0. \end{aligned} \tag{2.13}$$

$$\varphi'' + \frac{1}{2}Scf\varphi' - K_a Sce\left(\frac{\xi_a\epsilon_a}{\theta-\epsilon_a}\right)\varphi - Sc\xi\left(f'\frac{\partial\varphi}{\partial\xi} - \frac{\partial f}{\partial\xi}\varphi'\right) = 0. \tag{2.14}$$

The corresponding boundary conditions are

$$f'(\xi,0) = 1, \quad f(\xi,0) + 2\xi\frac{\partial f(\xi,0)}{\partial\xi} = 1, \quad \theta'(\xi,0) = -\frac{B_T}{\zeta_3}\Big[1-\theta(\xi,0)\Big], \quad \varphi(\xi,0) = 1. \tag{2.15}$$

$$f'(\xi,\infty)\to 0, \quad \theta(\xi,\infty)\to 0, \quad \varphi(\xi,\infty)\to 0. \tag{2.16}$$

The relevant non-dimensional parameters are

$$\begin{cases} \lambda_a = \dfrac{1}{\mu_f\omega_1\omega_2}, \quad \lambda_b = \dfrac{aU_\infty^2}{2\nu_f\omega_2^2}, \quad \mathcal{K} = \dfrac{\nu_f}{ak_m}, \\ \Delta_1 = \dfrac{\lambda_0 K_1\beta\rho_f}{2\pi\mu_f^2}(T_\infty - T_w), \quad \Delta_2 = \dfrac{a\mu_f^2}{\rho_f k_f(T_\infty - T_w)}, \\ B_T = \dfrac{h_f}{k_f}\sqrt{\dfrac{\nu_f}{a}}, \quad \alpha_a = \left(\dfrac{a}{\nu_f}\right)^{\frac{1}{2}}c, \quad P_r = \dfrac{(\mu c_p)_f}{k_f}, \\ R = \dfrac{4\sigma' T_\infty^3}{k' k_f}, \quad S_c = \dfrac{\nu_f}{D_B}, \quad \epsilon_a = \dfrac{T_\infty}{T_\infty - T_w}, \\ \xi_a = \dfrac{E_a}{R_a T_\infty}, \quad \Gamma_a = \dfrac{U_\infty^2}{a\nu_f}, \quad T_R = \dfrac{T_w}{T_\infty}, \\ K_a = \dfrac{K_r}{a}, \quad Ec = \dfrac{U_\infty^2}{(c_p)_f(T_w - T_\infty)}, \\ \zeta_1 = \dfrac{\mu_{hnf}}{\mu_f}, \quad \zeta_2 = \dfrac{\rho_{hnf}}{\rho_f}, \\ \zeta_3 = \dfrac{k_{hnf}}{k_f}, \quad \zeta_4 = \dfrac{(\rho c_p)_{hnf}}{(\rho c_p)_f}. \end{cases} \tag{2.17}$$

The names of the non-dimensional parameters appearing in equation (2.17) are presented in the subsequent Table 1.

From equation (2.17), $\zeta_1 = \dfrac{\mu_{hnf}}{\mu_f}$, $\zeta_2 = \dfrac{\rho_{hnf}}{\rho_f}$, $\zeta_3 = \dfrac{k_{hnf}}{k_f}$, $\zeta_4 = \dfrac{(\rho c_p)_{hnf}}{(\rho c_p)_f}$ are the nanofluid thermophysical properties.

Table 1 Non-dimensional Parameters and their Definition

Fluid Flow Parameter	Thermal Transport Parameter	Mass Transfer Parameter
λ_a, λ_b: fluid parameter	Δ_2: viscous dissipation	ξ_a: activation energy
$\mathcal{K}$: porosity parameter	B_T: Biot number	K_a: chemical reaction
Γ_a: dimensionless velocity	H_a, H_b: heat source	Sc: Schmidt number
α_a: dimensionless distance	P_r: Prandtl number	
Δ_1: ferrohydrodynamic	R: thermal radiation	
	T_R: temperature ratio	
	Ec: Eckert number	
	ϵ_a: Curie temperature	

The engineering physical parameters of interest are skin friction, Nusselt and Sherwood numbers, which are defined as Ogunseye and Sibanda (2019); Lawal et al. (2022)

$$C_f = \frac{\tau_w}{\frac{1}{2}\rho_f U_\infty^2}, \quad Nu_x = \frac{xq_a}{k_f(T_w - T_\infty)}, \quad Sh_x = \frac{xq_b}{D_B(C_w - C_\infty)}, \tag{2.18}$$

where the corresponding shear stress (τ_w), surface heat (q_a) and mass (q_b) fluxes are defined as

$$\tau_w = \left(\mu_{hnf} + \frac{1}{\omega_1\omega_2}\right)\frac{\partial u}{\partial y} - \frac{1}{6\omega_1\omega_2^3}\left(\frac{\partial u}{\partial y}\right)^3\Big|_{y=0}, \quad q_a = -\left(k_{hnf} + \frac{16\sigma' T^3}{3k'}\right)\frac{\partial T}{\partial y}\Big|_{y=0}, \quad q_b = -D_B\frac{\partial C}{\partial y}\Big|_{y=0}. \tag{2.19}$$

The dimensionless form of equation (2.18) using the non-similarity variable conversions (2.11) and (2.19) is given as

$$Re_x^{\frac{1}{2}}C_f = 2\left(\zeta_1(1+\lambda_a)f''(\xi,0) - \frac{\lambda_a\lambda_b}{3}(f''(\xi,0))^3\right), \quad Re_x^{-\frac{1}{2}}Nu_x = -\left(\zeta_3 + \frac{4R}{3}(1+(T_R-1)\theta(\xi,0))^3\right)\theta'(\xi,0), \quad Re_x^{-\frac{1}{2}}Sh_x = -\varphi'(\xi,0). \tag{2.20}$$

where $Re_x = \dfrac{U_\infty x}{\nu_f}$. The thermophysical properties are defined as follows (see Rawat et al. (2019)):

$$\begin{cases} \mu_{hnf} = \dfrac{1}{(1-\phi_1)^{2.5}(1-\phi_2)^{2.5}}\mu_f, \\ \rho_{hnf} = (1-\phi_2)[(1-\phi_1)\rho_f + \phi_1\rho_{p1}] + \phi_2\rho_{p2}, \\ \dfrac{k_{hnf}}{k_f} = \dfrac{k_{p2} + 2k_{bf} - 2\phi_2(k_{bf} - k_{p2})}{k_{p2} + 2k_{bf} + \phi_2(k_{bf} - k_{p2})}, \\ \dfrac{k_{bf}}{k_f} = \dfrac{k_{p1} + 2k_f - 2\phi_1(k_f - k_{p1})}{k_{p1} + 2k_f + \phi_1(k_f - k_{p1})}, \\ (\rho C_p)_{hnf} = (1-\phi_2)[(1-\phi_1)(\rho C_p)_f + \phi_1(\rho C_p)_{p1}] + \phi_2(\rho C_p)_{p2}. \end{cases} \tag{2.21}$$

The numerical values for the thermophysical properties of the base fluid and the nanoparticles are presented in Table 2.

Numerical Procedures

This section describes and implements the overlapping multi-domain bivariate SLLM to solve the dimensionless equations (2.12–2.14), which are subject to boundary conditions (2.15) - (2.16). Spectral collocation methods (SCMs) have been consistently recognized in the literature for yielding more accurate, computationally efficient, and rapidly convergent solutions when compared to conventional methods, including FEMs, Keller box technique, Runge–Kutta methods, and FDMs. The other benefits of SCMs include that they can be tailored to handle intricate nonlinear problems, which are characterized by complex geometries, material nonlinearity, and challenging boundary conditions.

Table 2 Thermophysical properties of the base-fluid and the hybrid nanoparticles (Aly and Pop 2019; Kumar et al. 2020)

	ρ	C_p	k
	kg/m^3	J/kgK	W/mK
Water	997.1	4179	0.613
Fe_2O_3	5180	670	9.7
Al_2O_3	3970	765	40

However, in the single-domain context, SCMs are limited to small computational domains. In large computational domains, using SCMs with large number of collocation points does not necessarily improve accuracy but instead the accuracy may be deteriorated. To overcome these limitations, recent studies (Mkhatshwa et al. 2020; Mkhatshwa 2024, 2022; Mkhatshwa and Khumalo 2023; Afridi et al. 2024) have introduced non-overlapping and overlapping grid strategies within spectral collocation frameworks to preserve accuracy, stability, and computational efficiency for both small and large domain problems. These improved approaches have proven to be highly effective for solving nonlinear boundary value problems (BVPs) which are similar to the one considered in this work. The method employed in the current scrutiny possess notable advantages, including ease of implementation for BVPs on semi-finite domains, high accuracy, rapid convergence, enhanced stability, which are all achieved using relatively few grid points. To initiate the solution procedure, the nonlinear PDEs (2.12) - (2.14) are linearized via the local linearization method (LLM), which implements univariate Taylor series expansion on the nonlinear equations, leading to a decoupled system of linear equations. Much like the Gauss-Seidel method utilized in linear system solvers, this approach assists in decoupling the system into smaller and manageable equations. Therefore, implementing the LLM algorithm on the nonlinear PDEs (2.12) - (2.14) yields the following linear iterative scheme:

$$a_{0,k}f'''_{k+1} + a_{1,k}f''_{k+1} + a_{2,k}f'_{k+1} + a_{3,k}f_{k+1} + a_{4,k}\frac{\partial f'_{k+1}}{\partial \xi} + a_{5,k}\frac{\partial f_{k+1}}{\partial \xi} = a_{6,k}, \tag{3.1}$$

$$b_{0,k}\theta''_{k+1} + b_{1,k}\theta'_{k+1} + b_{2,k}\theta_{k+1} + b_{3,k}\frac{\partial \theta_{k+1}}{\partial \xi} = b_{4,k}, \tag{3.2}$$

$$c_{0,k}\varphi''_{r+1} + c_{1,r}\varphi'_{r+1} + c_{2,r}\varphi_{r+1} + c_{3,r}\frac{\partial \varphi_{r+1}}{\partial \xi} = c_{4,r}, \tag{3.3}$$

where the subscripts k is used to indicates previous iteration level, $k+1$ corresponds to current iteration level, and the variable coefficients were derived through the implementation of the LLM algorithm. Suppose $\xi \in [0, \xi_F]$ represents the domain in the ξ-direction. Then, this interval is uniformly partitioned into r non-overlapping sub-intervals of equal length (see Fig. 2), each given by

$$J_\tau = [\xi_{\tau-1}, \xi_\tau], \tag{3.4}$$

where $\xi_0 = 0, \xi_r = \xi_F$, and $\tau = 1, 2, 3, ..., r$. Since the spectral collocation approach is inherently defined on $[-1, 1]$, it is necessary to transform each physical sub-interval $\xi \in [\xi_{\tau-1}, \xi_\tau]$ into the standard collocation interval $\hat{\xi} \in [-1, 1]$. The transformation is attained through the following linear mapping:

$$\hat{\xi} = \frac{2\xi}{\xi_\tau - \xi_{\tau-1}} - \frac{\xi_\tau + \xi_{\tau-1}}{\xi_\tau - \xi_{\tau-1}}. \tag{3.5}$$

This conversion is essential because it enables accurate spectral discretization and ensures that the method operates consistently throughout all sub-intervals $\tau = 1, 2, 3..., r$, regardless of their original position in the physical domain. To perform numerical approximation within each sub-domain in the ξ-direction, the solution domain is discretized using $(N_\xi + 1)$ Chebyshev-Gauss-Lobatto (C-G-L) nodes.

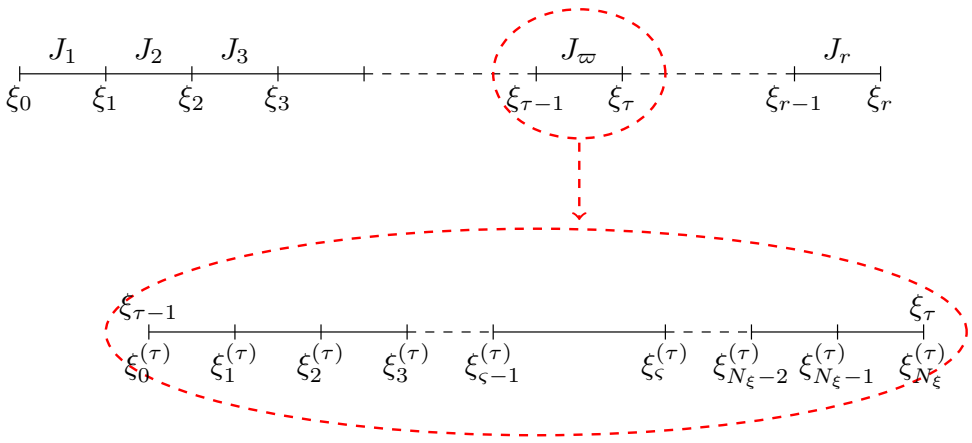


Fig. 2 Segmenting the ξ domain into r separate intervals without overlap

These collocation points ensure superior accuracy at the boundaries and are determined as follows Trefethen (2000):

$$\left\{\hat{\xi}_j\right\}_{j=0}^{N_\xi} = \cos\left(\frac{j\pi}{N_\xi}\right). \tag{3.6}$$

To minimize truncation errors associated with semi-infinite domains and to enable effective application of SCM, the semi-infinite domain $[0,\infty)$ in the $\eta-$direction, is approximated using a finite interval, which is denoted by $[0,\eta_\infty]$. This truncated domain is then partitioned into equally sized s sub-intervals that are overlapping, and each sub-interval has the following length:

$$L_s = \frac{\eta_\infty}{s+(1-s)(1-\cos(\pi/N_\eta))/2}. \tag{3.7}$$

Each sub-interval is expressed as follows (see Fig. 3):

$$K_\iota = [\eta_0^\iota, \eta_{N_\eta}^\iota], \quad \iota = 1,2,3...,s, \tag{3.8}$$

where $\eta_0^1 = 0$ and $\eta_{N_\eta}^s = \eta_\infty$. Again, $(N_\eta+1)$ C-G-L points are utilized in the discretization of each sub-interval in the $\eta-$direction. To ensure overlap between neighboring sub-domains, the last two collocation nodes of each sub-interval are designed to align exactly with the first two grid points of the subsequent sub-interval. Before applying SCM, each physical sub-interval $\eta \in [\eta_0^\iota, \eta_{N_\eta}^\iota]$ is linearly mapped into the standard collocation interval $\hat{\eta} \in [-1,1]$ through the following mapping:

$$\hat{\eta} = \frac{2\eta - (\eta_{N_\eta}^\iota + \eta_0^\iota)}{\eta_{N_\eta}^\iota - \eta_0^\iota}. \tag{3.9}$$

The associated collocation nodes in the ι^{th} sub-domain is expressed as in Trefethen (2000).

$$\{\hat{\eta}_l\}_{l=0}^{N_\eta} = \cos\left(\frac{l\pi}{N_\eta}\right). \tag{3.10}$$

To ensure global consistency, numerical computations are performed simultaneously throughout all sub-intervals in the η-direction. In contrast, the domain in the $\xi-$ direction is handled in a piece-wise manner, where each sub-interval is treated independently of the others. After attaining the solution at the last node of a sub-interval in the ξ-direction, the obtained numerical value is propagated forward as the initial condition in the subsequent sub-interval. This forward-marching scheme is repeated until the whole domain in the ξ-direction is covered. The initial value for the first sub-interval is attained by evaluating the system at $\xi = 0$, using the collocation point ξ_{N_ξ}. Consequently, the LLM scheme within each sub-interval $\tau = 1,2,3,...,r$, is independently expressed as follows:

$$\begin{aligned} &a_{0,k}\frac{\partial^3 \overset{(\tau)}{f}_{k+1}}{\partial\eta^3} + a_{1,k}\frac{\partial^2 \overset{(\tau)}{f}_{k+1}}{\partial\eta^2} + a_{2,k}\frac{\partial \overset{(\tau)}{f}_{k+1}}{\partial\eta} \\ &+ a_{3,k}\overset{(\tau)}{f}_{k+1} + a_{4,k}\frac{\partial}{\partial\eta}\left(\frac{\partial \overset{(\tau)}{f}_{k+1}}{\partial\xi}\right) \\ &+ a_{5,k}\frac{\partial \overset{(\tau)}{f}_{k+1}}{\partial\xi} = a_{6,k}, \end{aligned} \tag{3.11}$$

$$\begin{aligned} &b_{0,k}\frac{\partial^2 \overset{(\tau)}{\theta}_{k+1}}{\partial\eta^2} + b_{1,k}\frac{\partial \overset{(\tau)}{\theta}_{k+1}}{\partial\eta} + b_{2,k}\overset{(\tau)}{\theta}_{k+1} \\ &+ b_{3,k}\frac{\partial \overset{(\tau)}{\theta}_{k+1}}{\partial\xi} = b_{4,k}, \end{aligned} \tag{3.12}$$

$$\begin{aligned} &c_{0,k}\frac{\partial^2 \overset{(\tau)}{\varphi}_{k+1}}{\partial\eta^2} + c_{1,k}\frac{\partial \overset{(\tau)}{\varphi}_{k+1}}{\partial\eta} \\ &+ c_{2,k}\overset{(\tau)}{\varphi}_{k+1} + c_{3,k}\frac{\partial \overset{(\tau)}{\varphi}_{k+1}}{\partial\xi} = c_{4,k}. \end{aligned} \tag{3.13}$$

In the next step, the unknown functions and their associated derivative functions are approximated via the bivariate Lagrange interpolating polynomial, a technique thoroughly discussed in Mkhatshwa (2024, 2022); Mkhatshwa and Khumalo (2023); Afridi et al. (2024). These discrete functions and corresponding derivatives are then substituted

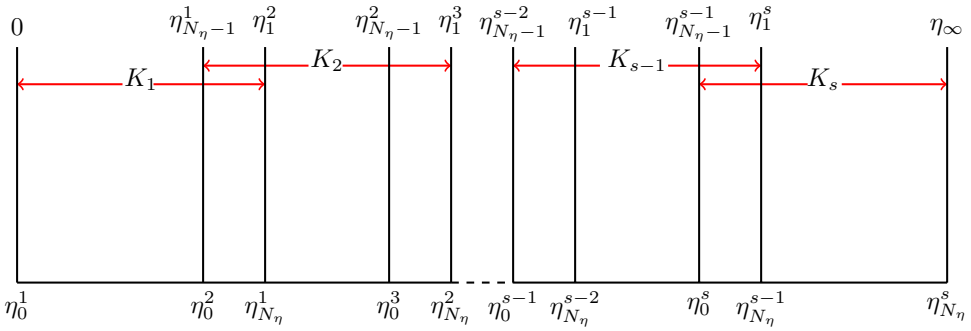


Fig. 3 Segmenting spatial domain into s subdomains that overlap with one another

into equations (3.11) - (3.13), and the spectral collocation approach is employed to obtain the required numerical solutions. With the initial conditions being incorporated, the resulting algebraic system takes the following discrete matrix form:

$$\begin{aligned}&\left[\boldsymbol{a}_{0,k}\mathrm{D}^3+\boldsymbol{a}_{1,k}\mathrm{D}^2+\boldsymbol{a}_{2,k}\mathrm{D}+\boldsymbol{a}_{3,k}\right]\overset{(\tau)}{\bar{\mathrm{F}}}_{i,k+1}\\&+\boldsymbol{a}_{4,k}\sum_{j=0}^{N_\xi-1}d_{i,j}\mathrm{D}\overset{(\tau)}{\bar{\mathrm{F}}}_{j,k+1}\\&+\boldsymbol{a}_{5,k}\sum_{j=0}^{N_\xi-1}d_{i,j}\overset{(\tau)}{\bar{\mathrm{F}}}_{j,k+1}=\overset{(\tau)}{\mathrm{R}}_{1,i,k},\end{aligned}\tag{3.14}$$

$$\begin{aligned}&\left[\boldsymbol{b}_{0,k}\mathrm{D}^2+\boldsymbol{b}_{1,k}\mathrm{D}+\boldsymbol{b}_{2,k}\right]\overset{(\tau)}{\bar{\boldsymbol{\Theta}}}_{i,k+1}\\&+\boldsymbol{b}_{3,k}\sum_{j=0}^{N_\xi-1}d_{i,j}\overset{(\tau)}{\bar{\boldsymbol{\Theta}}}_{j,k+1}=\overset{(\tau)}{\mathrm{R}}_{2,i,k},\end{aligned}\tag{3.15}$$

$$\begin{aligned}&\left[\boldsymbol{c}_{0,k}\mathrm{D}^2+\boldsymbol{c}_{1,k}\mathrm{D}+\boldsymbol{c}_{2,k}\right]\overset{(\tau)}{\bar{\boldsymbol{\varphi}}}_{i,k+1}\\&+\boldsymbol{c}_{3,k}\sum_{j=0}^{N_\xi-1}d_{i,j}\overset{(\tau)}{\bar{\boldsymbol{\varphi}}}_{j,k+1}=\overset{(\tau)}{\mathrm{R}}_{3,i,k},\end{aligned}\tag{3.16}$$

where $\overset{(\tau)}{\mathrm{R}}_{1,i,k}=\boldsymbol{a}_{6,k}-\boldsymbol{a}_{4,k}d_{i,N_\xi}\mathrm{D}\overset{(\tau)}{\bar{\mathrm{F}}}_{N_\xi}-\boldsymbol{a}_{5,k}d_{i,N_\xi}\overset{(\tau)}{\bar{\mathrm{F}}}_{N_\xi}$, $\overset{(\tau)}{\mathrm{R}}_{2,i,k}=\boldsymbol{b}_{4,k}-\boldsymbol{b}_{3,k}d_{i,N_\xi}\overset{(\tau)}{\bar{\boldsymbol{\Theta}}}_{N_\xi}$, and the structure of the $\overset{(\tau)}{\mathrm{R}}_{3,i,k}=\boldsymbol{c}_{4,k}-\boldsymbol{c}_{3,k}d_{i,N_\xi}\overset{(\tau)}{\bar{\boldsymbol{\varphi}}}_{N_\xi}$, derivative matrix D is well-documented in Mkhatshwa (2022); Mkhatshwa and Khumalo (2023). Each matrix equation yields a linear system involving $N_\xi(N+1)$ equations and same number of unknowns, where N indicates the total number of collocation points in the primary spatial domain, calculated as $N=N_\eta+(N_\eta+1)(s-1)$. For instance, equation (3.14) can be written in matrix form as

$$\begin{aligned}&\begin{bmatrix}\boldsymbol{\Omega}_{0,0}&\boldsymbol{\Omega}_{0,1}&\boldsymbol{\Omega}_{0,2}&\cdots&\boldsymbol{\Omega}_{0,N_\xi-1}\\\boldsymbol{\Omega}_{1,0}&\boldsymbol{\Omega}_{1,1}&\boldsymbol{\Omega}_{1,2}&\cdots&\boldsymbol{\Omega}_{1,N_\xi-1}\\\vdots&\vdots&\ddots&\vdots&\\\boldsymbol{\Omega}_{N_\xi-1,0}&\boldsymbol{\Omega}_{N_\xi-1,1}&\boldsymbol{\Omega}_{N_\xi-1,2}&\cdots&\boldsymbol{\Omega}_{N_\xi-1,N_\xi-1}\end{bmatrix}\begin{bmatrix}\overset{(\tau)}{\bar{\mathbf{F}}}_0\\\overset{(\tau)}{\bar{\mathbf{F}}}_1\\\vdots\\\overset{(\tau)}{\bar{\mathbf{F}}}_{N_\xi-1}\end{bmatrix}\\&=\begin{bmatrix}\overset{(\tau)}{\mathbf{R}}_{1,0}\\\overset{(\tau)}{\mathbf{R}}_{1,1}\\\vdots\\\overset{(\tau)}{\mathbf{R}}_{1,N_\xi-1}\end{bmatrix},\end{aligned}\tag{3.17}$$

where the dimension is $N_\xi(N+1)\times N_\xi(N+1)$, matrix entries are $\boldsymbol{\Omega}_{i,i}=\boldsymbol{a}_{0,k}\mathrm{D}^3+\boldsymbol{a}_{1,k}\mathrm{D}^2+\boldsymbol{a}_{2,k}\mathrm{D}+\boldsymbol{a}_{3,k}\mathrm{I}+\boldsymbol{a}_{4,k}d_{i,i}\mathrm{D}+\boldsymbol{a}_{5,k}d_{i,i}\mathrm{I}$ for $i=j$, and $\boldsymbol{\Omega}_{i,j}=\boldsymbol{a}_{4,k}d_{i,j}\mathrm{D}+\boldsymbol{a}_{5,k}d_{i,j}\mathrm{I}$ for $i\neq j$, I is the identity matrix of size $(N+1)\times(N+1)$. This matrix construction, consistent with equation (3.17), applies to the entire matrix equations (3.15) - (3.16). Boundary conditions are incorporated by modifying the respective rows in each diagonal block using values at the collocation nodes. The compact form of the full matrix system can be expressed as follows:

$$[\boldsymbol{\Omega}][\mathrm{F}]=[\mathrm{R}_1],[\boldsymbol{\Upsilon}][\boldsymbol{\Theta}]=[\mathrm{R}_2],[\boldsymbol{\Lambda}][\boldsymbol{\varphi}]=[\mathrm{R}_3].\tag{3.18}$$

Initial approximations are selected to start the iteration process and are designed in such a way that they conform to the corresponding boundary conditions.

Results and Discussion

To obtain the mathematical results, certain non-dimensional parameters were assigned specific values: $\xi=1,\ Pr=6.79,\ \lambda_a=0.5,\ \lambda_b=0.5,\ \Delta_1=0.2,\ \Delta_2=0.2, B_T=1.0,\ \alpha_a=0.8,\ \gamma_a=0.1,\ \gamma_b=0.1, R=1.2,\ \xi_a=0.5,\ \Gamma_a=1.0,\ T_R=1.2,\ K_a=0.8,\ Sc=1.0,\ \epsilon_a=1,\ Ec=0.5,\ \mathcal{K}=0.5,\ \phi_1=0.04,\ \phi_2=0.04$. These values were fixed in the entire numerical study, unless specified in the various figures. Table 3 presents numerical solutions of $f(\eta)$ for different values of η and $\mathcal{K}$, which are obtained using the overlapping grid-based SCM and the inbuilt MATLAB bvp4c solver. The comparative results are obtained when $\xi=Pr=\lambda_1=\lambda_b=\Delta_1=\Delta_2=\alpha_a=H_a=H_b=R=\xi_a=\Gamma_a=K_a=Sc=\epsilon_a=Ec=\phi_1=\phi_2=0$, $T_R=1$, and $B_T\to\infty$, and the mathematical model reduces to

$$f'''-\mathcal{K}f'+\frac{1}{2}ff''=0,\quad f'(0)=1,f(0)=1,f'(\infty)=0.\tag{4.1}$$

The set of results are in excellent agreement, thereby validating our current findings and further confirms that the proposed mathematical model accurately captures the underlying fluid flow, thermal and mass transfer mechanisms.

To assess the accuracy of the spectral (numerical) approach in approximating the full dynamical model, Fig. 4 presents the solution errors computed for the system of equations using varying numbers of sub-domains. The plot confirms that the method provides accurate approximations across the different configurations considered. Furthermore,

Table 3 Comparison of $f(\eta)$ for varying η and $\mathcal{K}$ values using overlapping grid-based SCM and bvp4c numerical solver

η	$\mathcal{K}=0$		$\mathcal{K}=0.1$		$\mathcal{K}=0.3$		$\mathcal{K}=0.5$	
	Present results	bvp4c solver	Present results	bvp4c solver	Present results	bvp4c solver	Present results	bvp4c solver
1.0	1.675001	1.675003	1.653166	1.653168	1.617455	1.617455	1.588861	1.588861
2.0	1.941775	1.941782	1.893790	1.893795	1.818215	1.818215	1.760456	1.760457
3.0	2.039660	2.039673	1.976781	1.976791	1.880036	1.880035	1.808179	1.808181
4.0	2.074553	2.074571	2.004729	2.004745	1.898744	1.898743	1.821275	1.821278
5.0	2.086848	2.086868	2.014059	2.014082	1.904374	1.904374	1.824854	1.824861
6.0	2.091149	2.091168	2.017159	2.017187	1.906065	1.906065	1.825832	1.825840
7.0	2.092636	2.092654	2.018180	2.018214	1.906571	1.906570	1.826098	1.826107
8.0	2.093134	2.093151	2.018508	2.018546	1.906719	1.906719	1.826170	1.826180
9.0	2.093284	2.093301	2.018605	2.018644	1.906760	1.906760	1.826188	1.826199
10	2.093313	2.093330	2.018623	2.018663	1.906768	1.906767	1.826192	1.826202

analysis shows that the combination of only two collocation points and 50 subdomains achieves the optimal convergence rate. The residual error plot presented in Fig. 5 supports the convergence trends illustrated in Fig. 4. The minimum residual error norms across all computed flow profiles (velocity, temperature, and concentration) were achieved using parameters $N = 2$ and $s = 50$. The magnitude of these residual errors, falling to approximately 10^{-14}, provides strong confidence in the accuracy and reliability of the numerical method employed.

The influence of the sheet void fraction (porosity parameter) $\mathcal{K}$ in the presence of a single (Al_2O_3) and hybrid nanoparticles (Al_2O_3 and Fe_2O_3) is displayed in Fig. 6. In line with the displayed graphs, increasing $\mathcal{K}$ dampen the velocity of the fluid. Whereas a contrary behaviour is noticed for the temperature and concentration distribution in both emulsification of a single and hybrid nanoparticles into the fluid. This increased resistance leads to a loss of momentum for the fluid, causing its velocity to decrease (dampen). The fluid has to work harder to move through or past the porous structure. When the fluid velocity is reduced, individual fluid particles spend a longer time in any given region, particularly near the stretching sheet. This extended contact time allows for more effective heat transfer, leading to a higher temperature within the fluid boundary layer. The thermal boundary layer thickens because heat can penetrate further into the slower-moving fluid. The slower fluid velocity allows more time for this species to diffuse. This results in a higher concentration of the species in the fluid. For Fig. 7, λ_a and λ_b are material parameter specific to the Eyring-Powell fluid model, which is a non-Newtonian fluid. These two parameters influence the fluid's rheological behaviour, often related to how its viscosity changes under shear stress. It is noted in Fig. 7 that increasing the Eyring-Powell fluid parameter λ_a enhances the fluid velocity, however, enhancing λ_b have a minimal retarding force on the fluid velocity. This is because the fluid is more viscous as λ_b is enhanced. We observed that the two fluid parameters have opposing behaviour on the fluid velocity.

The significance of the ferrohydrodynamic interaction parameter Δ_1 and the dimensionless distance parameter α_a on the velocity profiles of the fluid is shown in Fig. 8. Increasing the movement parameter α_a (from 0.6 to 1.0) leads to an increase in the fluid velocity. This implies that a larger α_a causes greater deceleration of the fluid flow within the boundary layer. Consequently, the velocity boundary layer thickness increases with increasing α_a. Ferrohydrodynamic (magnetic dipole)Δ_1 represents the strength of the interaction between the magnetic nanoparticles and the magnetic field gradient generated by the dipole. A positive Δ_1 indicates that the magnetic force (often referred to as the Kelvin force in this context) acts to decelerate the fluid velocity. Therefore, a stronger ferrohydrodynamic interaction do not enhances the fluid flow, resulting in a less thinner velocity boundary layer.

In Fig. 9, the influence of the Prandtl number in the range of [5, 15] and the Eyring-Powell fluid parameter λ_a in the range [0.1, 0.8] on the temperature profile is presented. As the Prandtl number (Pr) increases (from 5 to 15), the temperature profiles become steeper, and the temperature drops more rapidly with increasing distance η from the sheet. This means the thermal boundary layer thickness decreases with increasing Pr. Consequently, the thermal effect of the heated sheet is confined to a thinner region near the surface. This indicates that the fluid diffuse faster with the enhancement of the Prandtl number. Increasing the fluid parameter λ_a slightly increases the thermal boundary layer thickness, due to enhanced shear-thinning effects (reduced effective viscosity) allowing the fluid to carry heat further, however, away from the plate a counter effect can be observed as shown in Fig. 9. In Fig. 10, an increase in the dimensionless distance parameter leads to a decrease in the fluid's temperature.

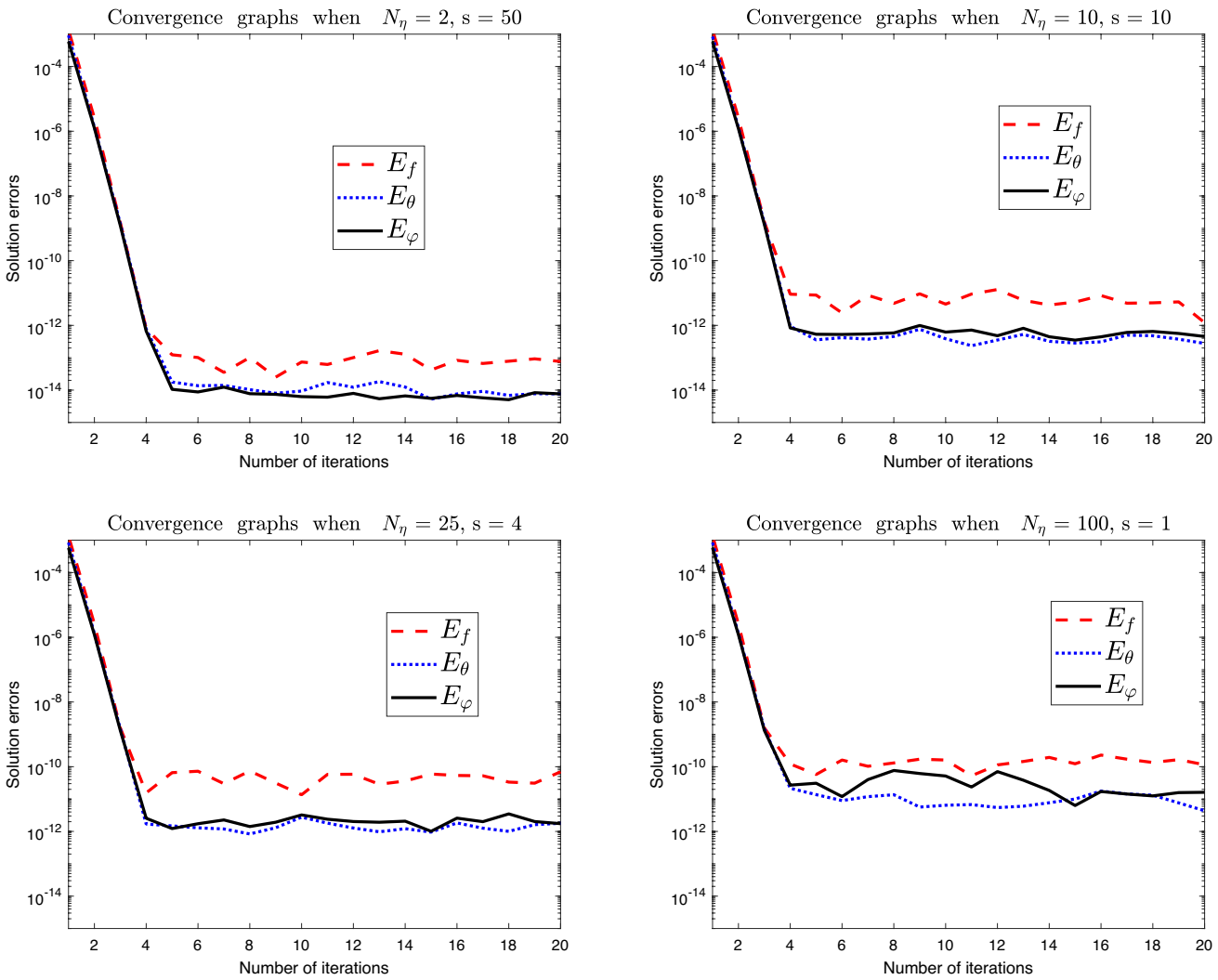


Fig. 4 Convergence graphs for different values of N_η and s

This results in lower temperatures deeper within the thermal boundary layer. The impact of Δ_1 on the fluid's temperature distribution over the stretching sheet is quite opposite to its effect on the fluid's velocity. The physical interpretation for the temperature trend with Δ_1 is that as fluid movement creates drag, more heat is generated. Thus, increasing trends in temperature are observed as the parametric value of Δ_1 increases.

Fig. 11 depicts the impact of radiation parameter (R) and Eckert number (Ec) on temperature profiles; we see how varying $R \in [0.4, 1.6]$ affects the temperature distribution of the fluid over the stretching sheet. Increasing R results in increasing temperature profiles, with the effect more pronounced before the fluid reached the far-field region. We note the effect of varying $Ec \in [0.0, 0.6]$ on temperature profiles. Higher Eckert numbers correspond to increased temperatures, representing greater viscous dissipation effects converting kinetic energy into thermal energy.

The influence of the space-dependent H_a and temperature-dependent H_b heat source parameters on the fluid temperature is displayed in Fig. 12. Higher positive values of H_a yield higher temperature profiles, indicating increased heat generation in the fluid. Positive H_b values (heat generation) increase fluid temperature, while negative values (heat absorption) decrease it. The largest temperature differences are observed near the boundary region.

In Fig. 13, a high Biot number (B_T) contributes to high temperature profiles close to the surface of the sheet and reduces drastically due to the wide temperature difference. Biot number helps in various thermal processing application such as food processing and material processing. The temperature ratio which is a dimensionless quantity which represents the ratio of surface temperature to the ambient temperature is depicted in Fig. 13. We observed that higher temperature ratio results in high temperature profiles except close to the sheet at $\eta = 0$. This stronger potential drives a

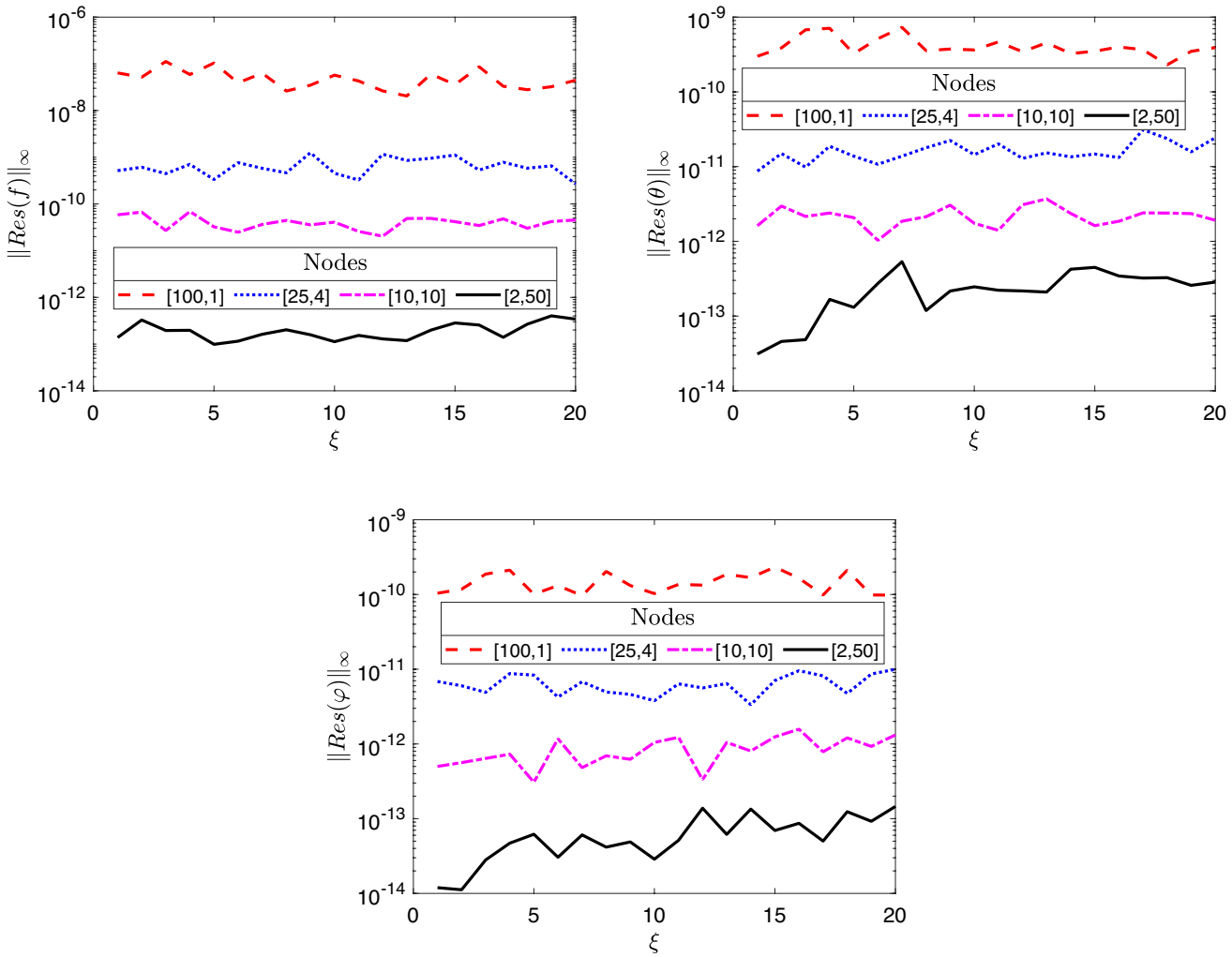


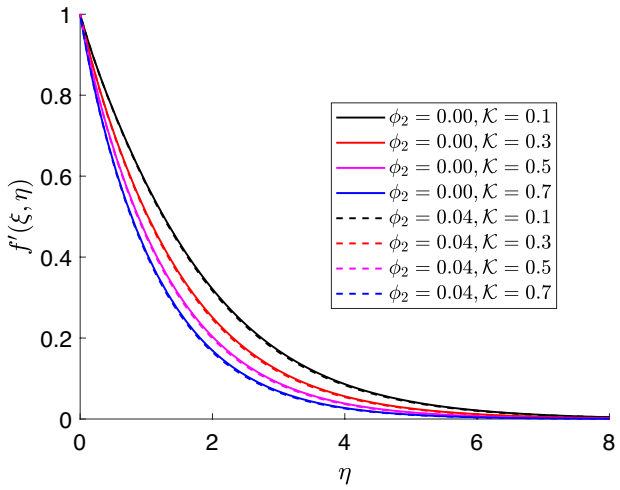
Fig. 5 Residual error graphs for different values of N and q

greater heat flux from the wall into the fluid. To carry this increased heat away from the surface, the fluid within the thermal boundary layer must attain higher temperatures compared to a situation with a lower temperature ratio. Therefore, the entire temperature profile within that affected region is elevated.

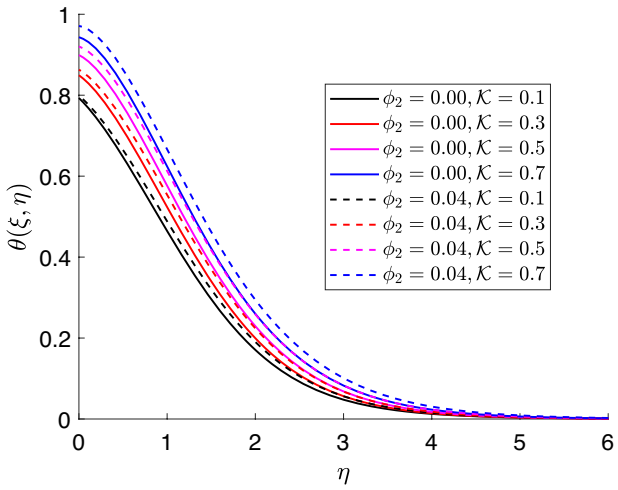
Fig. 14 displays that increase in Schmidt number reduced the concentration by showing steeper concentration gradient and a thinner concentration boundary layer reason being that larger Schmidt number leads to lower mass diffusivity; thereby the concentration is left at a reduced level. It is seen in Fig. 14 that increasing the space generation/absorption parameter results in higher concentration of the species thereby increasing the concentration profiles. Furthermore, in Fig. 14 the increase in heat generation parameter has been found to increase the reaction rate leading to faster consumption of reactants and formation of products.

It is observed in Fig. 15 that the concentration profiles decrease as the rate of chemical reaction parameter increases. This behaviour is realistic in that when the rate of chemical reaction parameter increases, the reaction in the system is expected to be faster, and the concentration of the system is therefore reduced as reactant species are depleted in the process. Activation energy plays a crucial role in determining the rate of chemical reactions and their profiles, subsequently, the concentration of reactants and products. Reducing the activation energy increases the reaction rate and automatically leads to higher concentrations of products and profiles.

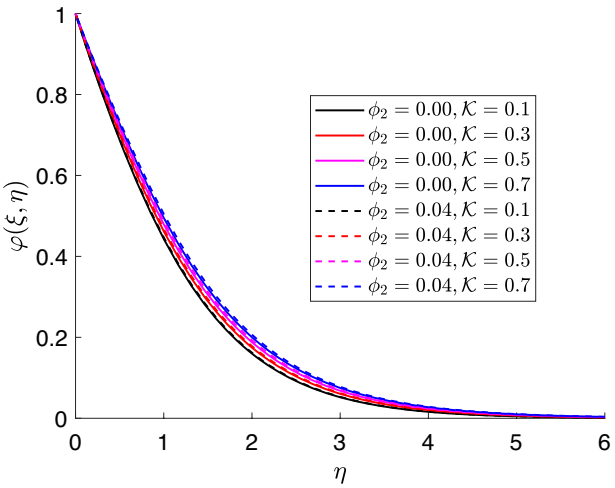
The influence of having a nanofluid to hybrid nanofluid and ferrohydrodynamic parameter is displayed in Fig. 16. As the nanoparticle volume fraction ϕ_2 increases (from 0 to 0.04), the curves shift upwards (become less negative). This indicates that increasing the concentration of nanoparticles decreases the magnitude of the skin friction coefficient (reduces drag). This result is somewhat counter-intuitive, as adding nanoparticles generally increases the effective viscosity of the fluid. Higher viscosity typically leads to higher



(a) Velocity profiles

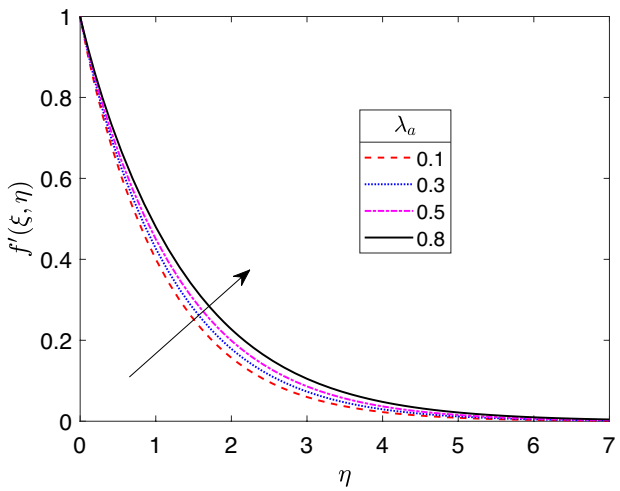


(b) Temperature profiles



(c) Concentration profiles

Fig. 6 Impact of ϕ_2 and $\mathcal{K}$ on the flow profiles



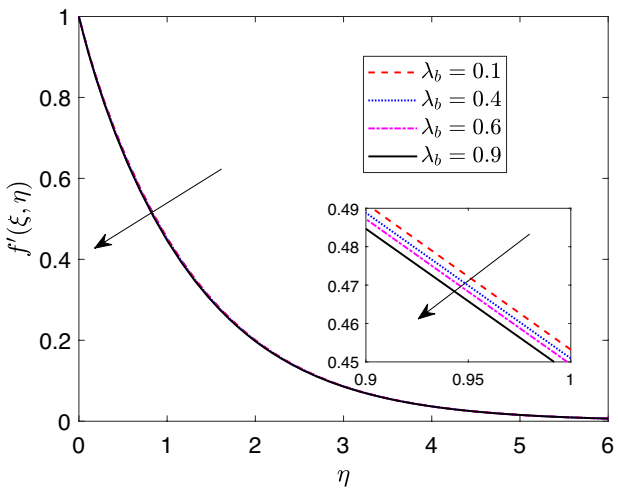


Fig. 7 Impact of λ_a and λ_b on velocity profiles

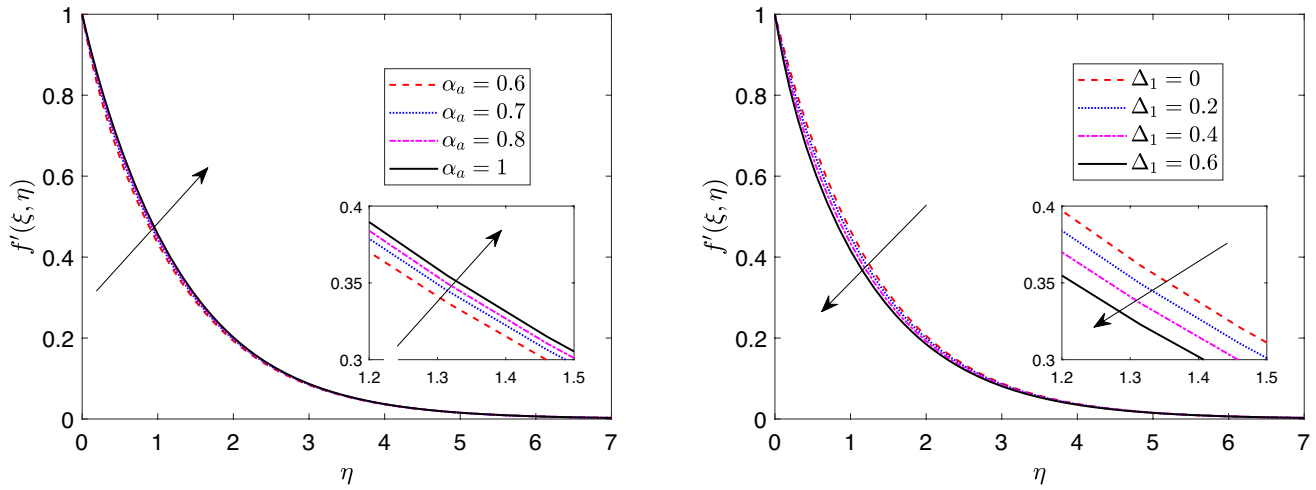


Fig. 8 Impact of α_a and Δ_1 on velocity profiles

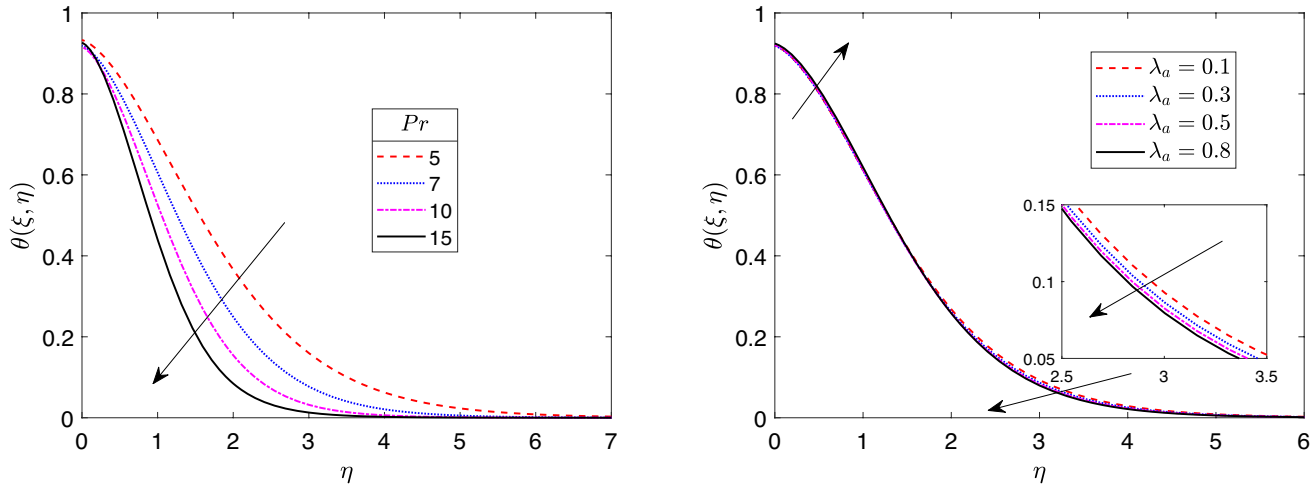


Fig. 9 Impact of Pr and λ_a on temperature profiles

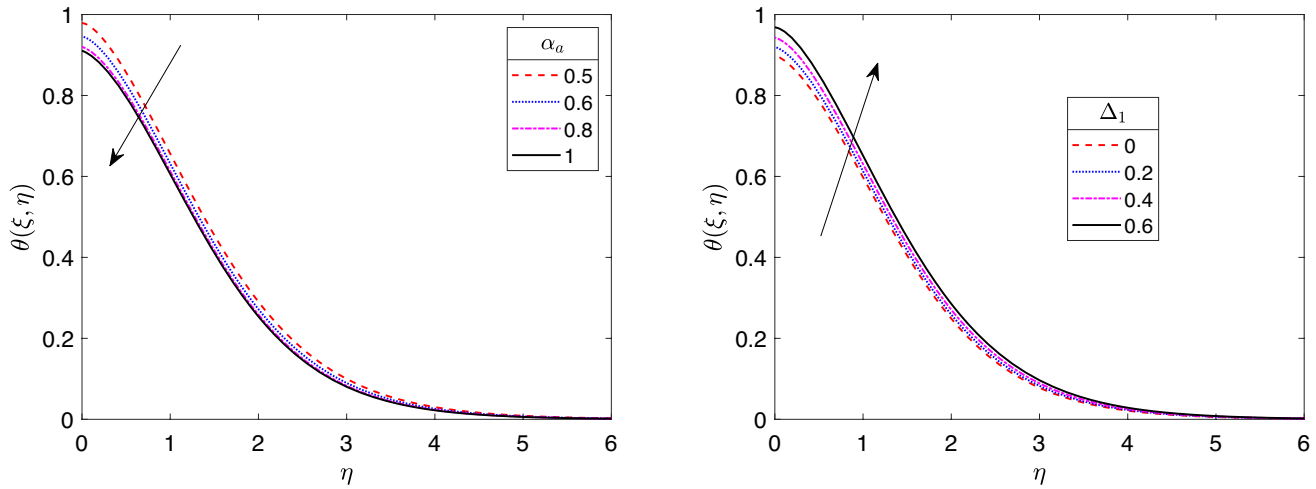


Fig. 10 Impact of α_a and Δ_1 on temperature profiles

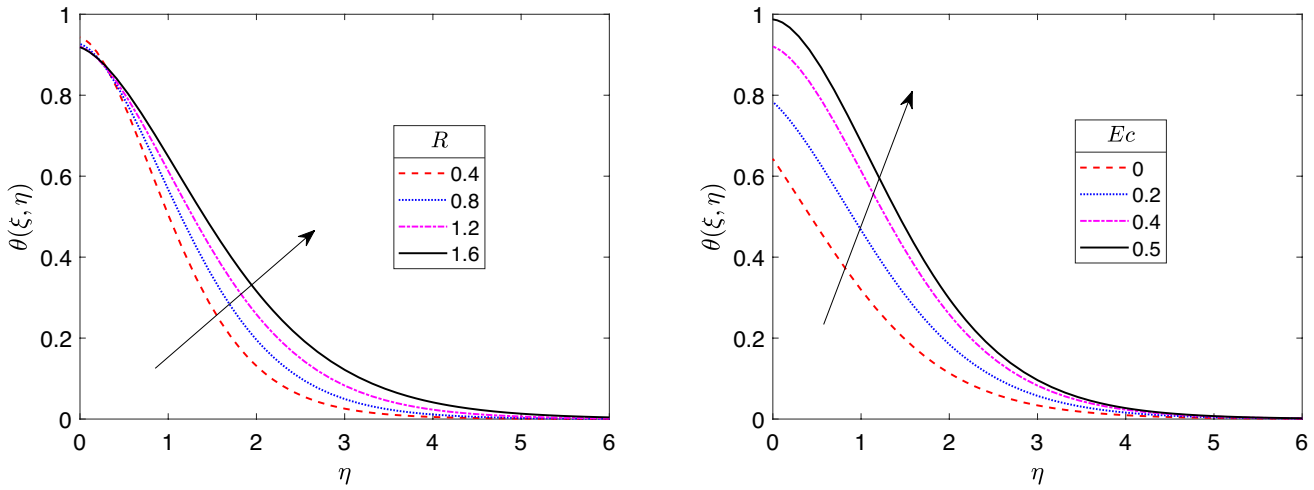


Fig. 11 Impact of R and Ec on temperature profiles

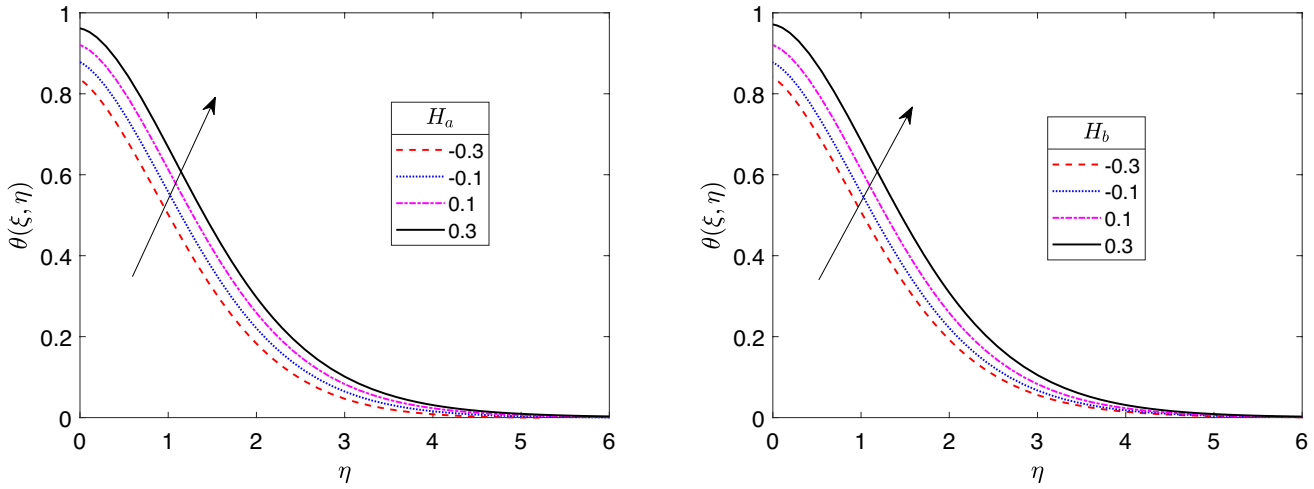


Fig. 12 Impact of H_a and H_b on temperature profiles

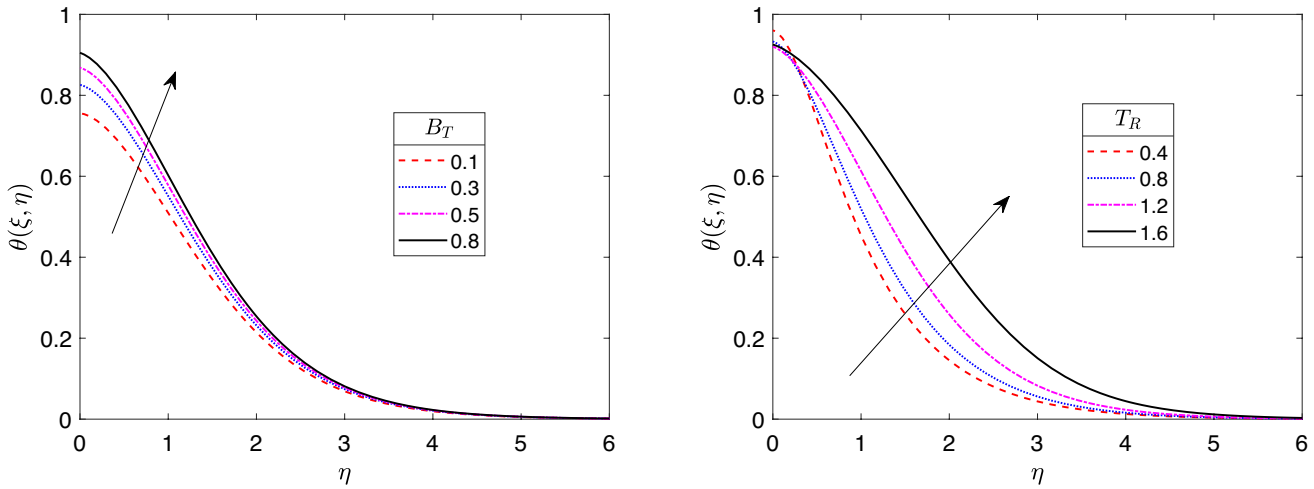


Fig. 13 Impact of B_T and T_R on temperature profiles

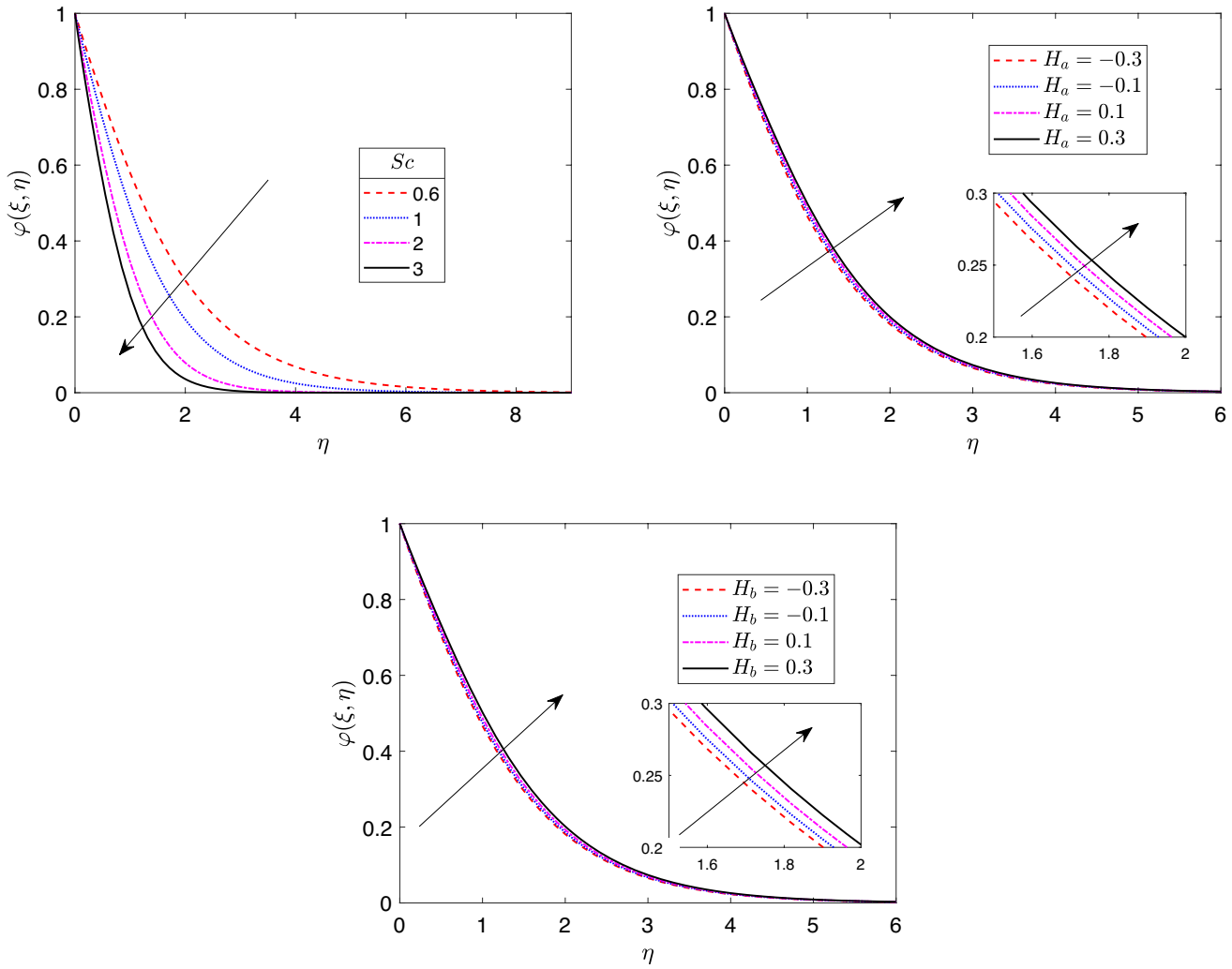


Fig. 14 Impact of Sc, H_a and H_b on concentration profiles

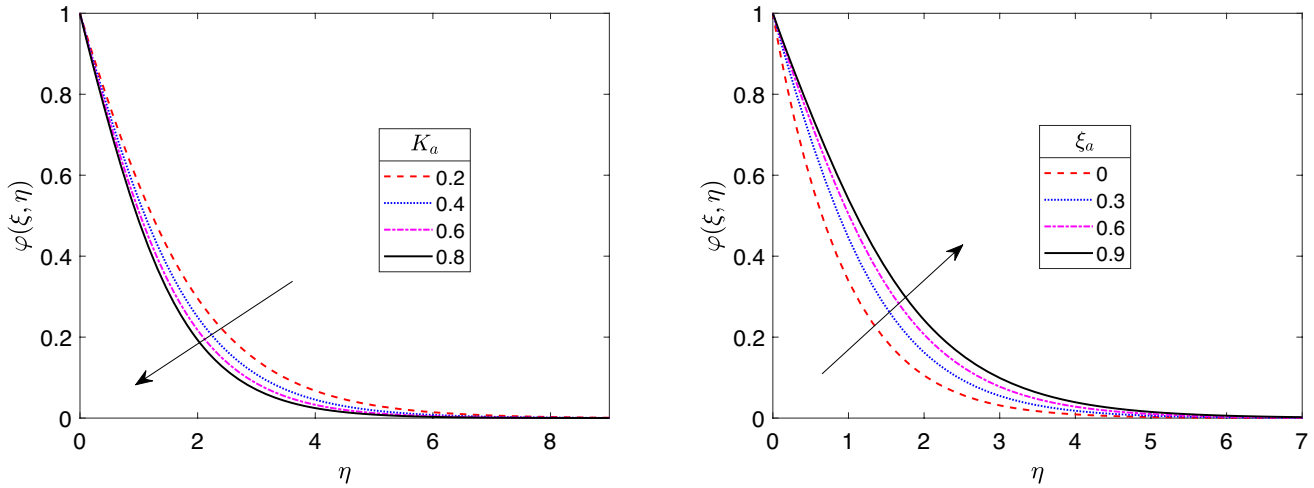


Fig. 15 Impact of K_a and ξ_a on concentration profiles

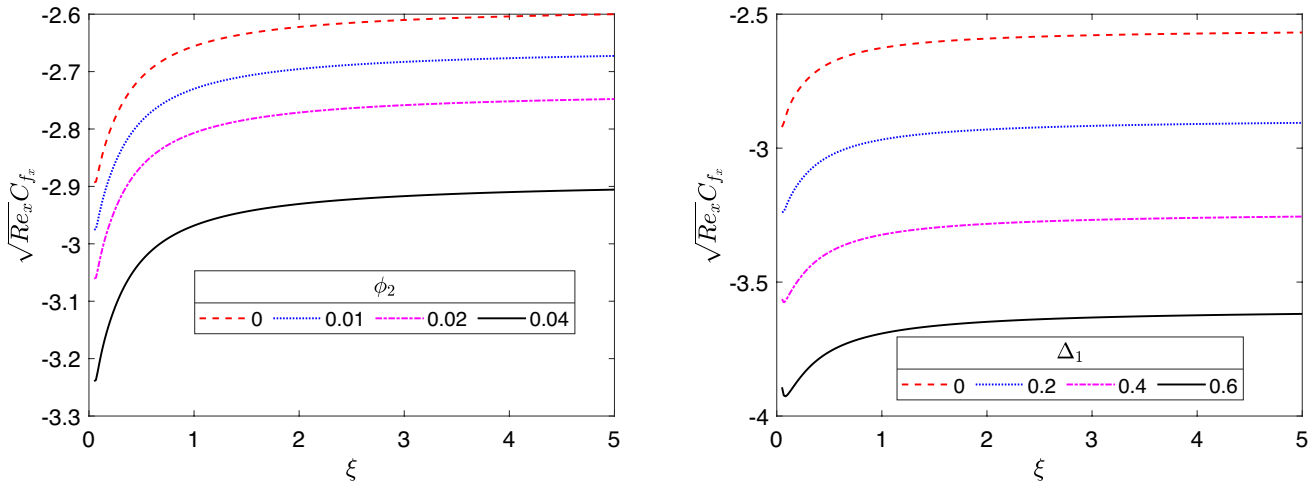


Fig. 16 Impact of ϕ_2, $\mathcal{K}$ and Δ_1 on skin friction coefficient

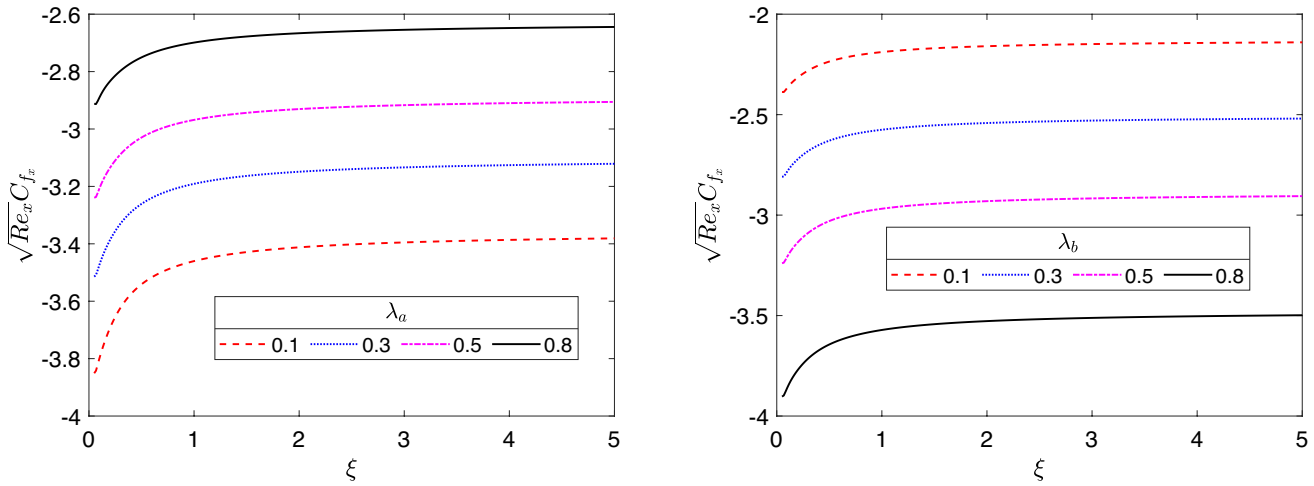


Fig. 17 Impact of λ_a and λ_b on skin friction coefficient profiles

shear stress and thus higher skin friction. The observed trend suggests that, in this specific system, factors leading to drag reduction outweigh the expected increase from viscosity enhancement. Increasing the ferrohydrodynamic effect strongly decreases the magnitude of the skin friction (reduces drag). The influence of the the fluid parameters λ_a and λ_b at the wall is contrasting. We observed that increasing λ_a leads to enhancement in the drag force across the dimensionless streamwise coordinate. Whereas, increment in λ_b reduces the drag of the fluid at $y = 0$, see Fig. 17.

Fig. 18 presents the influence of distance and porosity parameter on the skin friction which decreases with distance from the leading edge as the boundary layer thickens. Higher Porosity which gives rise to higher permeability reduces the skin friction. In Fig. 19, as the dimensionless distance increases from 0.6 to 1.0, the plots consistently moves upward with lesser value along ξ. This means that for any given location ξ, the value of $Re_x^{-\frac{1}{2}} Nu_x$ increases for a higher value of α_a is experienced. Increasing the Curie temperature parameter ϵ_a also decreases heat transfer, likely by weakening beneficial thermomagnetic convection or through flow stabilization/retardation effects caused by the magnetic forces under those specific thermal conditions. Increasing the effect of viscous dissipation decreases the heat transfer rate (decreases the Nusselt number). This acts as non-internal heat source within the boundary layer. When Δ_2 increases, this internal heating becomes less significant. This reduces the temperature of the fluid layers close to the wall and subsequently the heat transfer rate, see Fig. 20. Similar behaviour exhibited by Δ_2 is observed by Δ_1 on the rate of heat transfer rate.

In Fig. 21 as the thermal radiation parameter R increases (from 0.4 to 1.6), the Nusselt number value significantly shoot upwards. R quantifies the relative importance of thermal radiation as a mode of heat transfer compared to

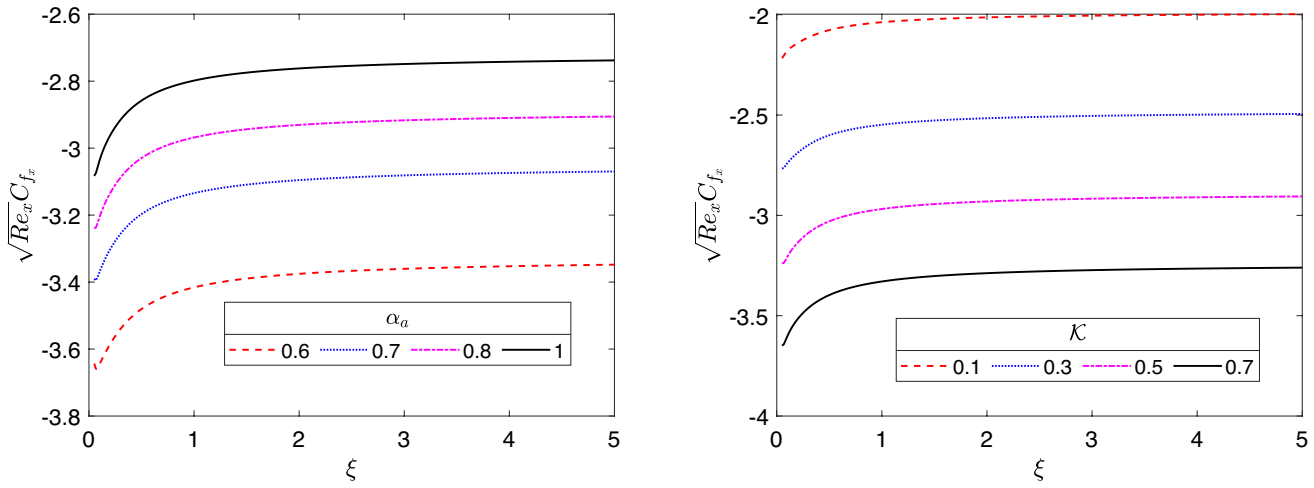


Fig. 18 Impact of α_a and $\mathcal{K}$ on skin friction coefficient profiles

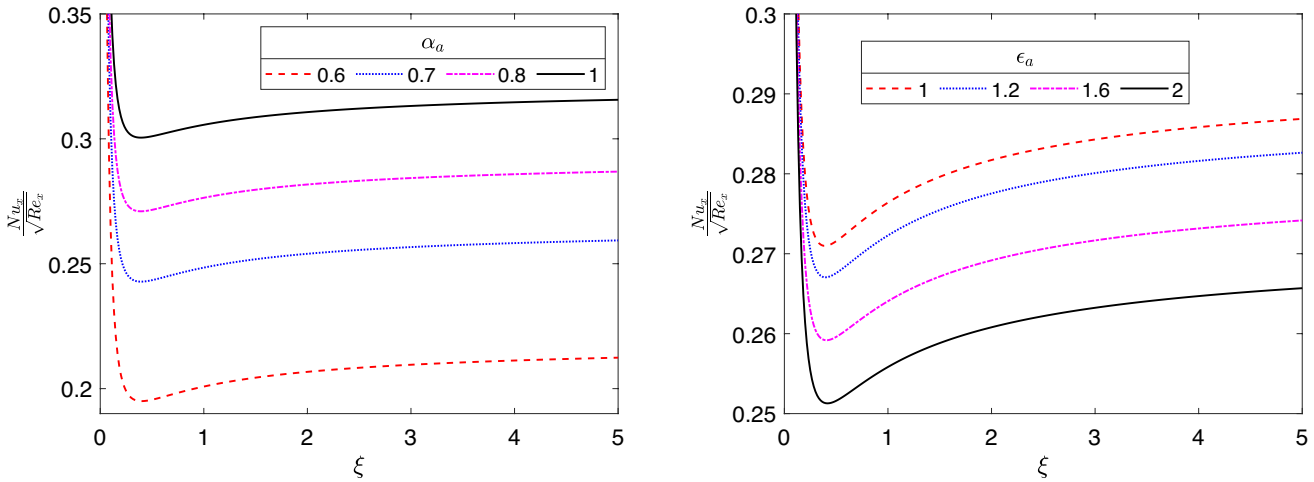


Fig. 19 Impact of α_a and ϵ_a on heat transfer rate

conduction/convection. Thermal radiation allows energy to be transported directly from the hotter surface through the fluid. By providing an additional pathway for heat to leave the surface, radiation effectively cools the surface region more efficiently (or heats the bulk fluid more readily). This process leads to a steeper temperature gradient near the wall. A steeper gradient corresponds to a higher heat flux and therefore a higher Nusselt number. However, increasing the Eckert number reduces the heat transfer rate (decreases the Nusselt number). A higher *Ec* signifies more intense internal heating of the fluid due to viscous friction. This raises the fluid temperature within the boundary layer, reduces the temperature difference between the wall and the adjacent fluid, makes the temperature gradient at the wall less steep, and consequently decreases the heat flux from the wall, leading to a lower Nusselt number. The behaviour of the Biot number and temperature ratio on the heat transfer rate is depicted in Fig. 22. Increasing B_T and T_R support the heat transfer rate of the fluid. The increase in Schmidt number is found to contribute to the increase in the rate of mass transfer in the flow dynamical system as presented in Fig. 23. It is also shown that porosity affects mass transfer rate in the system by influencing the available surface area and allowing more fluid to flow through the porous medium. Importantly, the hybrid nanofluid has less mass transfer coefficient compared to the nanofluid. In Fig. 24, the increase in the rate of chemical reaction parameter contribute to the increase in Sherwood number. In the same vein, increase in activation energy reduces the rate of mass transfer.

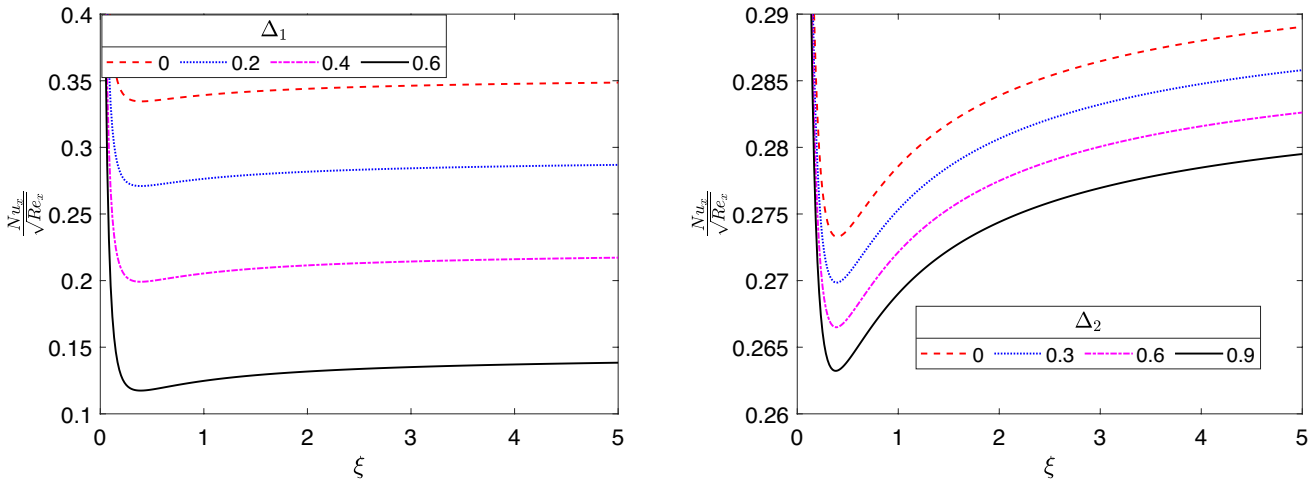


Fig. 20 Impact of Δ_1 and Δ_2 on heat transfer rate

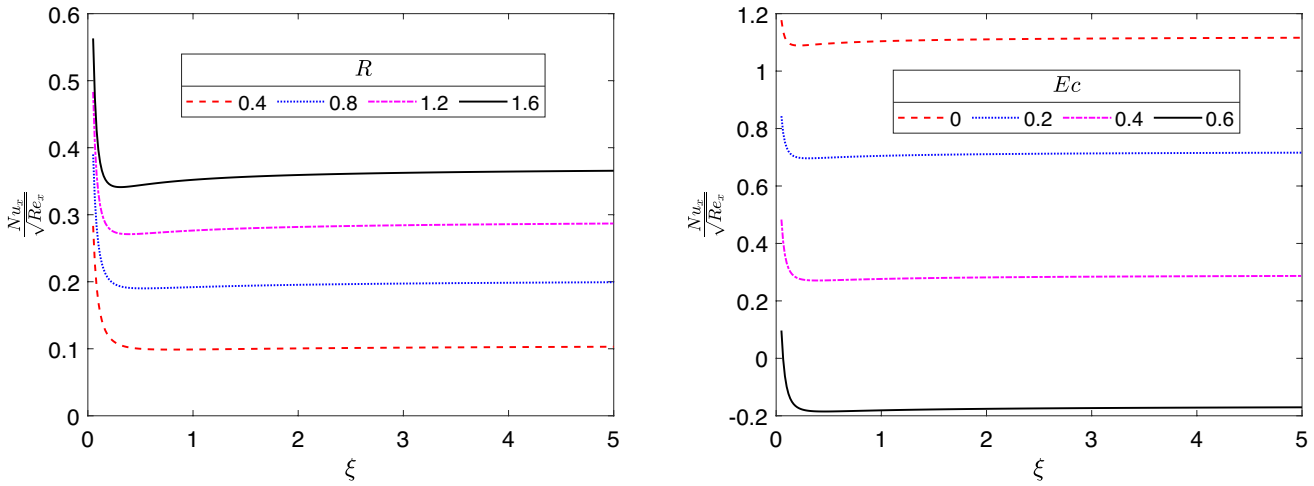


Fig. 21 Impact of R and Ec on heat transfer rate

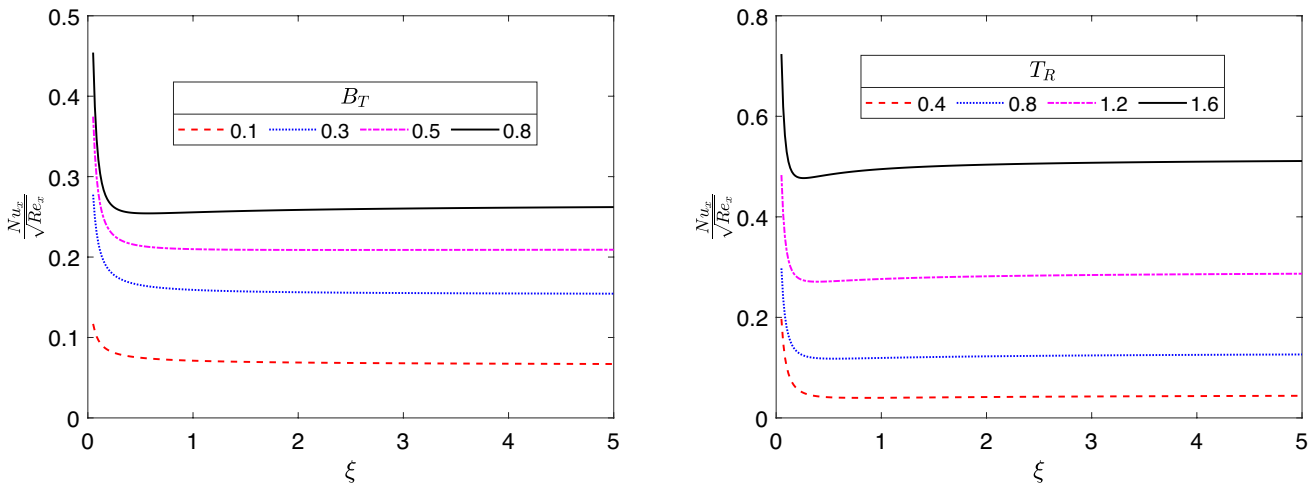


Fig. 22 Impact of B_T and T_R on heat transfer rate

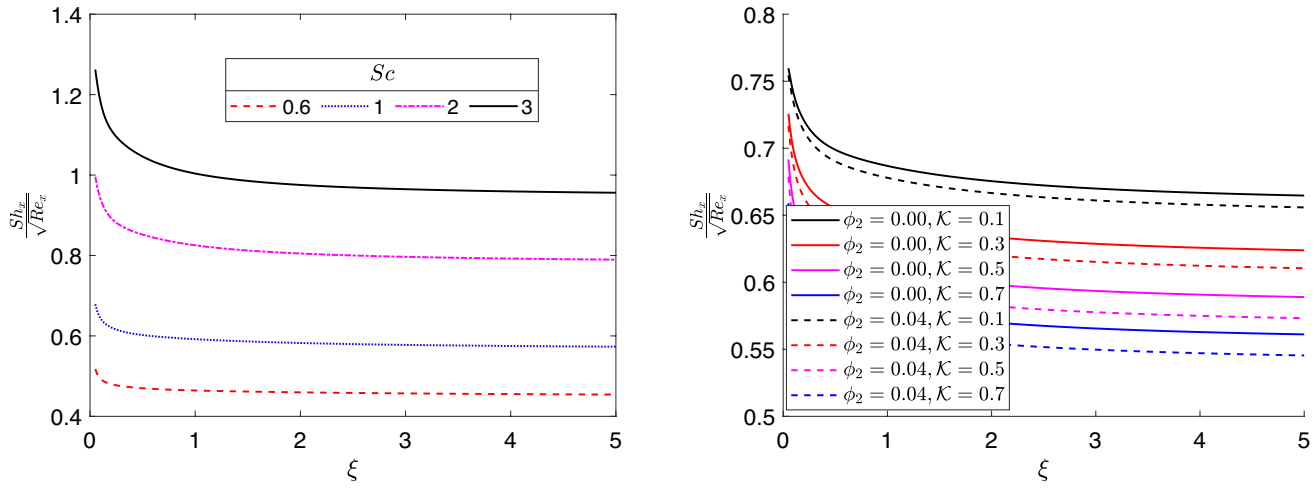


Fig. 23 Impact of Sc and $\mathcal{K}$ on mass transfer rate

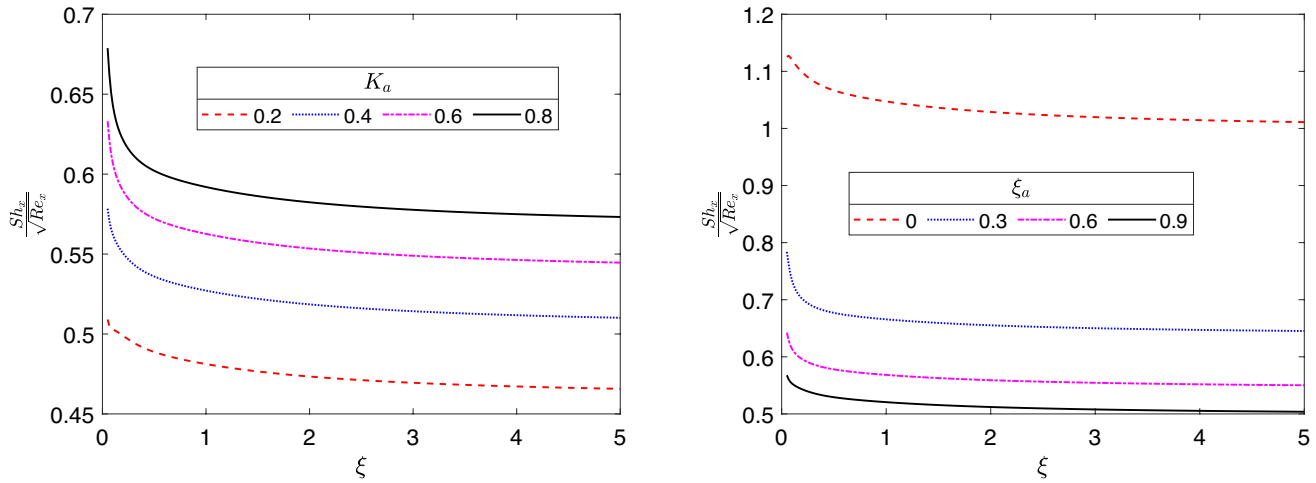


Fig. 24 Impact of K_a and ξ_a on mass transfer rate

Conclusions

A numerical simulation of the steady, two-dimensional boundary layer phenomenon of an Eyring-Powell hybrid nanofluid over an expanding surface, considering the influence of a magnetic dipole. The complex system of governing partial differential equations was effectively transformed using a set of non-similar group of transformation, to dimensionless two-variable deterministic equation. The resulting non-linear, coupled system was then solved with high accuracy using the efficient spectral overlapping multidomain collocation method. The reliability and convergence of the employed numerical scheme were carefully validated through detailed analysis of solution and residual errors plots, affirming the credibility of the obtained results. We systematically explored the impact of various pertinent physical parameters on the fluid's velocity, temperature, and nanoparticle concentration distributions, along with crucial engineering quantities like the skin friction coefficient, Nusselt number, and Sherwood number. The findings of this study include the following:

- Variations in Eyring-Powell fluid parameters lead to differentiated and opposing alterations of the surface drag force.
- The efficiency of heat dissipation from the sheet's surface is improved by increasing either the Biot number or the thermal radiation parameter.
- Heat generation have a great influence on the movement of the fluid and heat distribution. The temperature-dependent heat source have more influence compared to the spatial-dependent heat source.
- The negative impact of increased viscosity on convection outweighs the positive impact of enhanced thermal conductivity, especially at the wall.

- In this specific flow system, factors leading to drag reduction outweigh the expected increase from viscosity enhancement.

Overall, this work contributes to a deeper understanding of the complex interplay between non-Newtonian fluid mechanics, magnetic dipole effects, hybrid nanoparticle enhancement, and boundary layer phenomena over stretching surfaces. The detailed numerical results and insights presented herein are valuable for the design and optimization of industrial processes involving advanced fluids and thermal management systems, and demonstrate the capability of the spectral overlapping technique in handling such intricate fluid dynamics problems. In future research, the authors are looking forward to exploring the applications of this phenomenon in different coordinate geometries. It will also be interesting to explore the significance of more than two nanoparticles to obtain maximum energy efficiency.

Acknowledgments The authors would like to express their heartfelt gratitude to the Tertiary Education Trust Fund (TETFund) for their generous sponsorship of this research. This support has facilitated the smooth execution, implementation, and early completion of this project. We are thankful for the opportunity it has provided to the academic community. TETFund Reference Number: TETF/DR\&D/CE/UNIV/ONDO/IBR/2024/VOL.1.

Author contributions KBK: Conceptualization, Writing—Original Draft and Final Draft MOL: Conceptualization, iscussion of results, Reviewing and Editing, Supervision MPM: Methodology, Formal analysis, Reviewing and Editing, Software, Supervision YOT: Conceptualization, Formal analysis, Reviewing and Editing, Writing—Original and Final Draft OO: Methodology, Discussion of results, Reviewing and Editing, Supervision

Funding Open access funding provided by Rhodes University.

Data availability No datasets were generated or analysed during the current study.

Declarations

Conflict of interest The authors declare no Conflict of interest.

Open Access This article is licensed under a Creative Commons Attribution 4.0 International License, which permits use, sharing, adaptation, distribution and reproduction in any medium or format, as long as you give appropriate credit to the original author(s) and the source, provide a link to the Creative Commons licence, and indicate if changes were made. The images or other third party material in this article are included in the article's Creative Commons licence, unless indicated otherwise in a credit line to the material. If material is not included in the article's Creative Commons licence and your intended use is not permitted by statutory regulation or exceeds the permitted use, you will need to obtain permission directly from the copyright holder. To view a copy of this licence, visit http://creativecommons.org/licenses/by/4.0/.

References

Adomian G (1994) Solving frontier problems of Physics: The decomposition method. Kluwer Academic Publishers

Afridi MI, Mkhatshwa MP, Qasim M, Chamkha AJ (2024) Thermal and computational analysis of MHD dissipative flow of Eyring-Powell fluid: Nonl-similar approach via overlapping grid-based spectral collocation scheme. Chin J Phys 92:1026–1042

Akolade MT, Tijani YO (2021) A comparative study of three dimensional flow of casson–williamson nanofluids past a riga plate: spectral quasi-linearization approach. Part Differ Equ Appl Math 4:100–108

Aly EH, Pop I (2019) MHD flow and heat transfer over a permeable stretching/shrinking sheet in a hybrid nanofluid with a convective boundary condition. Int J Numer Methods Heat Fluid Flow 28:3012–3038. https://doi.org/10.1108/HFF-12-2018-0794

Ansari MS, Otegbeye O, Trivedi M, Goqo SP (2021) Magnetohydrodynamic bio-convective Casson nanofluid flow: a numerical simulation by paired quasilinearisation. J Appl Comput Mech 7(4):2024–2039

Awgichew G, Kebeke T, Haile E, Walelign T (2020) Heat and mass transfer in unsteady boundary layer flow of williamson nanofluids. J Appl Math 13

Canuto C, Hussaini MY, Quarteroni A, Zang TA (2006) Spectral Methods: Fundamentals in Single Domains. Springer-Verlag, Berlin

Choi US (1995) Enhancing thermal conductivity of fluids with nanoparticles, developments and application of non-Newtonian flows. ASME J Heat Transfer 66:99–105

Choudhary P, Loganathan K, Jat K, Sharma K, Eswaramoorthi S (2025) Shape factor analysis of water and aluminium oxide nanoparticles in a porous medium with slip effects. Chem Phys Impact 10:100882

Devi SU, Devi SA (2017) Heat transfer enhancement of $Cu - Al_2O_3$ /water hybrid nanofluid flow over a stretching sheet. J Nigerian Math Soc 36:419–433

Gholinia M, Gholinia S, Hosseinzadeh K, Ganji DD (2018) Investigation on ethylene glycol nano fluid flow over a vertical permeable circular cylinder under effect of magnetic field. Result Phys 9:1525–1533

Gontijo RG, Cunha FR (2017) Numerical simulations of magnetic suspensions with hydrodynamic and dipole-dipole magnetic interactions. Phys Fluids 29:062004

Haile E, Seid E, Walelign T (2022) Multiple slip, soret and dufour effects in fluid flow near a vertical stretching sheet in the presence of magnetic nanoparticles. Int J Thermofluids 13

Hayat T, Ahmad S, Khan IM, Alsaedi A (2003) Exploring magnetic dipole contribution on radiative flow of ferromagnetic Williamson fluid. Results Phys 8:545–551

Ibrahim W, Lamesse T (2023) Powell-Eyring nanofluid analysis with finite element method when past stretching sheet with convective heating and passive control of nanoparticle. Int J Thermofluids 19:100388

Ireka IE (2015) Computational analysis of non-isothermal flow of non-Newtonian fluids. PhD thesis, University of Cape Town

Jat K, Sharma K, Choudhary P, Soni P (2025) Bioconvection of a radiating and reacting nanofuid fow past a nonlinear stretchable permeable sheet in a porous medium. J Biol Phys 51:18

Jat K, Sharma K, Choudhary P, Soni P (2025) Entropy generation analysis of couple stress casson fluid flow through non-permeable stretching channel. Eur Phys J. https://doi.org/10.1140/epjs/s11734-025-01525-y

Javed T, Ali N, Abbas Z, Sajid M (2013) Flow of an eyring-powell non-newtonian fluid over a stretching sheet. Chem Eng Commun 200(3):327–336

Kasali KB, Ajadi SO (2025) Heat and mass transfer behaviour of an mhd elastico-viscous nanofluid over a rotating disk with viscous dissipation, radiation, and heat source. J Nanofluids 14:16–26

Kumar KA, Sandeep N, Sugunamma V, Animasaun IL (2020) Effect of irregular heat source/sink on the radiative thin film flow of MHD hybrid ferrofluid. J Therm Anal Calorim 139:2145–2153

Kundu PK, Cohen IM, Dowling DR (2016) Fluid mechanics Academic Press 6:1–921

Lawal MO, Kasali KB, Ogunseye HA, Oni MO, Tijani YO, Lawal YT (2022) On the mathematical model for Erying-Powell nanofluid flow with Brownian and thermophoresis effects in the presence of heat source and chemical reaction. Partial Differ Equ Appl Math 5:100318

Liao S (2012) Beyond perturbation: Introduction to the homotopy analysis method. Chapman andHall/CRC Press, Boca Raton

Magagula M, Motsa VSS, Sibanda P (2020) On the bivariate spectral quasilinearization method for nonlinear boundary layer partial differential equations. Editor(s): R.O. Fagbenle, O.M. Amoo, S. Aliu, A. Falana. In Woodhead Publishing Series in Energy. Applications of Heat, Mass and Fluid Boundary Layers, Woodhead Publishing. https://doi.org/10.1016/B978-0-12-817949-9.00016-5.

Makinde OD, Chinyoka T (2013) Numerical investigation of buoyancy effects on hydromagnetic unsteady flow through a porous channel with suction/injection. J Mech Sci Technol 27(5):1557–1568

Mkhatshwa MP (2022) Overlapping grid spectral collocation approach for electrical MHD bioconvection Darcy-Forchheimer flow of a Carreau-Yasuda nanoliquid over a periodically accelerating surface. Heat Transfer 51:1468–1500

Mkhatshwa MP (2024) Overlapping grid-based spectral collocation technique for bioconvective flow of MHD Williamson nanofluid over a radiative circular cylindrical body with activation energy. Computation 12:75

Mkhatshwa MP, Khumalo M (2023) Double diffusion and Hall effects on MHD sinusoidal natural convection flow of silver water-based nanofluid from a porous vertical plate. Partial Differ Equ Appl Math 7:100516

Mkhatshwa MP, Motsa SS, Ayano MS, Sibanda P (2020) MHD mixed convective nanofluid flow about a vertical slender cylinder using overlapping multi-domain spectral collocation approach. Case Stud Thermal Eng 18:100598

Motsa SS (2015) On the new bivariate local linearisation method for solving coupled partial differential equations in some applications of unsteady fluid flows with heat and mass transfer. Editor: M. Solecki. IntechOpen. Mass Transfer: Advancement in Process Modelling, Woodhead Publishing

Motsa SS (2013) A new spectral local linearization method for nonlinear boundary layer flow problems. J Appl Math 2013(1):423628

Nahlia MK, Sinha S, Loganathan K, Jat K, Choudhary P (2025) Numerical computation of magnetohydrodynamic maxwell fluid flow with mixed convection and heat source effects across an inclined exponential stretching surface. Partial Differ Equ Appl Math 14:101169

Odenbach S (2003) Magnetic fluids-suspensions of magnetic dipoles and their magnetic control. J Phys Condens Matter 15:S1497

Ogunseye HA, Sibanda P (2019) A mathematical model for entropy generation in a Powell-Eyring nanofluid flow in a porous channel. Heliyon 5(5):e01662. https://doi.org/10.1016/j.heliyon.2019.e01662

Ogunseye HA, Tijani YO, Sibanda P (2020) Entropy generation in an unsteady Eyring-Powell hybrid nanofluid flow over a permeable surface: a lie group analysis. Heat Transf 49(6):3374–3390

Ogunseye HA, Salawu SO, Fatunmbi EO (2021) A numerical study of MHD heat and mass transfer of a reactive Casson-Williamson nanofluid past a vertical moving cylinder. Partial Differ Equ Appl Math 4:100148

Otegbeye O, Goqo SP, Ansari MS (2020) Comparative study of some spectral based methods for solving boundary layer flow problems. AIP Conf Proc 2253:020013

Rawat SK, Yaseen M, Khan U, Kumar M, Eldin SM, Alotaibi MA, Galal AM (2019) Significant of non-uniform heat source/sink and Cattaneo-Christov model on hybrid nanofluid flow in a Darcy-Forchheimer porous. Front Mater 9:1097057

Sandeep N, Sulochana C (2018) Momentum and heat transfer behaviour of Jeffrey, maxwell and oldroyd-b nanofluids past a stretching surface with non-uniform heat source/sink. Ain Shams Eng J 9(4):517–524. https://doi.org/10.1016/j.asej.2016.02.008

Takemitsu N (1985) Finite difference method to solve incompressible fluid flow. J Comput Phys 61(3):499–518

Tijani YO, Oloniiju SD, Kasali KB, Akolade MT (2022) Nonsimilar solution of a boundary layer flow of a reiner–philippoff fluid with nonlinear thermal convection. Heat Transf 51(6):5659–5678

Tijani YO, Adeosun AT, Ogunseye HA, Niranjan H (2023) Magnetic dipole dynamics on Reiner-Philippoff boundary layer flow. Numer Heat Transf Part A Appl 85(10):1691–1705

Tijani YO, Akolade MT, Otegbeye O, Yusuf A (2023) Surface dynamics on Jeffrey nanofluid flow with Coriolis effect and variable Darcy regime. J Appl Math Mech 104(2):e202300217

Trefethen Lloyd N (2000) Spectral methods in MATLAB. SIAM

Vaishnav BK, Choudhary S, Choudhary P, Jat K, Loganathan K, Eswaramoorthi S (2025) Computational analysis of radiative micropolar fuid fow over a curved stretching sheet with viscous dissipation. Discover Appl Sci 7:451

Wajihah SA, Sankar DS (2023) A review on non-newtonian fluid models for multi-layered blood rheology in constricted arteries. Arch Appl Mech 93:1771–1796

Waleign A, Kebeke T, Haile E, Walelign T (2020) Analytical study of heat and mass transfer in unsteady mhd radiant flow of williamson nanofluid over stretching sheet with heat generation and chemical reaction. Heat Transfer 49:4246–4263

Walelign T, Seid E (2024) Mathematical model analysis for hydromagnetic flow of micropolar nanofluid with heat and mass transfer over inclined surface. Int J Thermofluids 21:100541

Walelign T (2025) Analysis of casson nanofluid transport rates near a vertical stretching sheet with dissipation and slip effects. Front Appl Math Stat. 11:1526769

White FM (2006) Viscous fluid flow. Third ed New York McGraw-Hill 1:1–250

Zeeshan A, Majeed A, Ellahi R (2016) Effect of magnetic dipole on viscous ferro-fluid past a stretching surface with thermal radiation. J Mol Liq 215:549–554

Publisher's Note Springer Nature remains neutral with regard to jurisdictional claims in published maps and institutional affiliations.